J. Fluid Mech. (1999), *vol.* 390, *pp.* 45–73. Printed in the United Kingdom

Stability analysis of natural convection in a cavity; walls with uniform heat or mass flux

By L.-G. SUNDSTRÖM† AND M. VYNNYCKY

Department of Mechanics, Royal Institute of Technology (KTH), S-100 44 Stockholm, Sweden

(Received 20 February 1998 and in revised form 14 January 1999)

A linear stability analysis is made of a family of natural convection flows in an arbitrarily inclined rectangular enclosure. The flow is driven by prescribed heat or mass fluxes along two opposing walls. The analysis allows for perturbations in arbitrary directions; however, the purely longitudinal or transverse modes are numerically found to be the most unstable. For the numerical treatment, a finite difference method with automatically calculated differencing molecules, variable order of accuracy, and accurate boundary treatment is developed. In cases with boundary layers, a special scaling is applied.

For base solutions with natural (bottom heavy) stratification, critical conditions are solved for as a function of the Rayleigh number, Ra, and the angle of inclination to the bottom-heated case, α, for different Prandtl numbers (Pr), with complete results for $Pr = 0.025, 0.1, 0.7, 7, 1000$, and $Pr \to \infty$. The uniform flux case is found to be much more stable than that of Hart (1971) with fixed wall temperatures, a fact which is attributed to the much larger stratification which occurs in the base solution. As could be expected, instabilities tend to be favoured by a decrease in Pr, an increase in Ra, and a decrease in α; however, exceptions to all these rules could be found.

Cases in which the wavenumber is zero, or approaches zero in different ways, are studied analytically. Integral conditions, derived from the unresolved end regions, are applied in the analysis. The results show that all the base solutions with unnatural (top heavy) stratification are unstable to large-wavelength stationary rolls whose axes are parallel with the base flow.

Real-valued perturbations are constructed and visualized for some of the modes considered.

1. Introduction

Stability analysis is concerned with investigating under what conditions given solutions to nonlinear differential equations are stable in time. From the pioneering work of Lord Rayleigh (1916), and up to the present, fluid flows have been a major object of study. Three very useful textbooks on stability in fluid flows are Chandrasekhar (1961), Joseph (1976) and Drazin & Reid (1981). The last one contains both a very readable overview of the field and a detailed literature review. In the following, we present a small selection of work on stability of natural convection in enclosures, with the intention to put the present work into context.

For the Rayleigh–Bénard case of a bottom-heated horizontal enclosure, Pellew

† L.-G. Sundström died during the publication process of this paper. Correspondence should be directed to M. Vynnycky.

& Southwell (1940) made a structured presentation of the basic problem and gave an accurate solution for the bifurcation from a conductive solution to one with convection in the form of stationary rolls. This first bifurcation occurs at Rayleigh numbers, based on the wall-to-wall distance and temperature difference, of 1708 for the uniform temperature case and 720 for the uniform flux case (Sparrow, Goldstein & Jonsson 1963). Finite box sizes have a stabilizing effect, as shown by Davis (1967). For subsequent bifurcations, the criticality conditions also depend on the Prandtl number. The review by Busse (1978) reports extensive stability results. There, the wavelength of the base-flow rolls was varied as an independent parameter. Five different modes were found to define the stability boundary in the (Ra, Pr, wavenumber)-space. Experiments, in which active control of the wavenumber was exercised, have provided some verification. Koschmieder (1993, chaps. 6 and 7) considers the wavenumber to be a unique function of Ra and Pr, and criticizes the works summarized in Busse (1978) for varying the wavelength too freely. However, unless the stability boundaries from Busse (1978) should actually be incorrect, the amendments indicated by Koschmieder merely amount to picking out a subset of those results – which would still be an important addition, if valid.

The stability for a side-heated vertical enclosure was investigated by Birikh *et al.* (1969), who prescribed the wall temperatures T_1+Sx and T_2+Sx (x being the vertical coordinate), and solved for $Pr = 0.2, 1$, and 5. The stratification constant S was varied as a free parameter, but was kept fairly small in the study. For cases with weak natural stratifications, monotonic instabilities were found to be dominant (we believe that the more common term 'stationary instability' may sound like a contradiction for people outside the field). Boundary layers arise for larger stratifications, and were treated by Gill & Davey (1969), who solved in the boundary-layer approximation only, but for a wider range of Prandtl numbers. Travelling-wave instabilities were found in all their cases. Bergholz (1978) verified the travelling-wave instabilities from Gill & Davey (1969), but also found monotonic instabilities to be effective in two parameter regions: for $Pr < 12.7$ and weak stratification, in agreement with Birikh *et al.* (1969), and for $Pr > 50$ and stronger stratification. The latter modes had not been investigated in previous theoretical work, but were found to agree well with experiments by Elder (1965) and Vest & Arpaci (1969).

An arbitrarily inclined enclosure with side walls of uniform temperatures and a naturally occurring stratification was treated by Hart (1971), both theoretically, for $Pr = 0.71$ and $Pr = 6.7$, and experimentally, for $Pr = 6.7$ (water). For the vertical case, Hart observed travelling waves only, which was explained by the fact that the stratification which occurs naturally at steady-state is, even for the case of uniform wall temperatures, too large for the low-Pr stationary instabilities found by Birikh *et al.* (1969) to occur. We shall later return to the work of Hart (1971) for comparison with our own findings.

The present work concerns the case in which the heat (or mass) flux, rather than the temperature (or concentration), is prescribed on the walls. Our interest in the case arose from electrochemical cells, where the desirable property of a uniform current distribution leads to a condition of uniform ionic flux. An exact base solution for the case was recently found by Sundström & Kimura (1996, hereafter referred to as SK), who combined a generalized version of the solutions given by Hart (1971) with a strict control volume method for determining the stratification from the end-region boundary conditions, the latter originating from a physical argument in Bejan (1979). Near the Bénard limit, multiple solutions were found to exist; one branch has a natural stratification, and is accompanied by a varying number of branches with

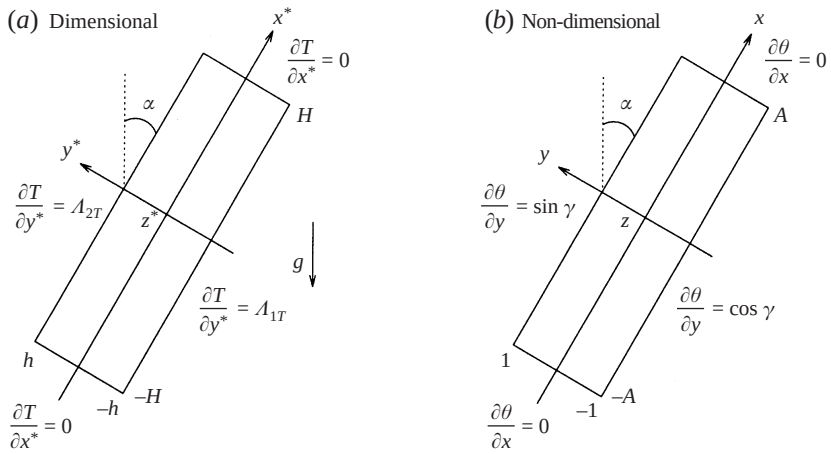

FIGURE 1. Geometry and coordinate system.

unnatural stratification. It is shown in Appendix A that the unnatural solutions are always unstable; consequently, most of the present work is devoted to investigating the stability of the natural solutions. For those, we attempt to treat perturbations of arbitrary nature for continuously varying inclination angles, and to do this for sufficiently many values of Pr so that the general behaviour of the stability boundaries of the different modes is made clear.

2. Non-dimensional variables and equations

With the geometry given by figure 1, the following non-dimensional variables are defined:

$$t = \frac{t^* k}{\rho c_p h^2}, \quad x = \frac{x^*}{h}, \quad y = \frac{y^*}{h}, \quad z = \frac{z^*}{h}, \tag{2.1a–d}$$

$$\theta = \frac{T - T_0}{\Lambda_T h}, \quad \boldsymbol{u} = \frac{\nu \boldsymbol{u}^*}{\beta_T \Lambda_T h^3 g}, \quad p = \frac{p^*}{\beta_T \Lambda_T \rho h^2 g}, \tag{2.1e–g}$$

$$Ra = \frac{\beta_T \Lambda_T h^4 g \rho c_p}{\nu k}, \quad Pr = \frac{\nu \rho c_p}{k}, \quad A = \frac{H}{h}, \quad A_z = \frac{H_z}{h}, \quad \lambda_1 = \frac{\Lambda_{1T}}{\Lambda_T}, \quad \lambda_2 = \frac{\Lambda_{2T}}{\Lambda_T}, \tag{2.1h–m}$$

where $\Lambda_T = \sqrt{\Lambda_{1T}^2 + \Lambda_{2T}^2}, \quad \Lambda_{1T} = -\dfrac{q''(y=-1)}{k}, \quad \Lambda_{2T} = -\dfrac{q''(y=1)}{k}.$ (2.1 *n–p*)

T_0 is the average initial temperature, q'' the heat flux, β_T the coefficient of thermal expansion, k the heat conductivity, c_p the specific heat capacity, ν the kinematic viscosity, ρ the fluid density, and g the gravitational acceleration. The scaling is such that the dimensionless fluxes λ_1 and λ_2 are restricted to lie on the curve $\lambda_1^2 + \lambda_2^2 = 1$, so that one can write

$$\lambda_1 = \cos\gamma, \quad \lambda_2 = \sin\gamma, \tag{2.2a, b}$$

where γ is the angle in the (λ_1, λ_2)-plane. These are the same definitions as in SK, with the addition of a third coordinate direction, z, and a box width in that direction, H_z. The corresponding definitions for an equivalent mass transfer case can be found in

that work. The governing equations are

$$\frac{1}{Pr}\left(\frac{\partial \boldsymbol{u}}{\partial t} + Ra\,(\boldsymbol{u}\cdot\nabla)\boldsymbol{u}\right) = -\nabla p + \nabla^2\boldsymbol{u} + \theta\cos\alpha\boldsymbol{e}_x + \theta\sin\alpha\boldsymbol{e}_y, \tag{2.3}$$

$$\nabla\cdot\boldsymbol{u} = 0, \tag{2.4}$$

$$\frac{\partial\theta}{\partial t} + Ra\,\boldsymbol{u}\cdot\nabla\theta = \nabla^2\theta, \tag{2.5}$$

with the boundary conditions that $\boldsymbol{u} = 0$ on all the boundaries, and that

$$\left.\frac{\partial\theta}{\partial y}\right|_{y=-1} = \lambda_1, \quad \left.\frac{\partial\theta}{\partial y}\right|_{y=1} = \lambda_2, \quad \left.\frac{\partial\theta}{\partial x}\right|_{x=\pm A} = 0, \quad \left.\frac{\partial\theta}{\partial z}\right|_{z=\pm A_z} = 0. \tag{2.6a–d}$$

However, the full problem will not be treated. Instead of applying the boundary conditions on the endwalls in the x- and z-directions, we solve for a region which does not extend all the way to those walls. This must be done with some caution: if the x and z walls are far away, we would not expect the details of what goes on there to matter for the interior. However, no matter how far away the walls are, one must take care not to violate global conservation of mass and energy. Rather than to ensure this by actually solving the end regions as well and matching the solutions to the interior, we shall employ a different method, following SK, which makes use of control volumes whose bounding surfaces are partly attached to the boundaries where the original boundary conditions are given, and partly cut through the region solved for. The method is particularly simple to apply for cases in which the fluxes are prescribed.

With a control volume which has $y \in [-1, 1]$, $x \in [-A, x_0]$, and $z \in [-A_z, z_0]$, where x_0 and z_0 are arbitrary, one obtains, using the boundary conditions on the x and z walls, the following integral conditions:

$$\int_{-A_z}^{z_0}\int_{-1}^{1} u(x_0, y, z)\,\mathrm{d}y\,\mathrm{d}z + \int_{-A}^{x_0}\int_{-1}^{1} w(x, y, z_0)\,\mathrm{d}y\,\mathrm{d}x = 0, \tag{2.7}$$

$$\int_{-A}^{x_0}\int_{-A_z}^{z_0}\int_{-1}^{1}\frac{\partial\theta}{\partial t}\,\mathrm{d}y\,\mathrm{d}z\,\mathrm{d}x + \int_{-A_z}^{z_0}\int_{-1}^{1}\left(Rau\theta - \frac{\partial\theta}{\partial x}\right)_{x=x_0}\mathrm{d}y\,\mathrm{d}z + \int_{-A}^{x_0}\int_{-1}^{1}\left(Raw\theta - \frac{\partial\theta}{\partial z}\right)_{z=z_0}\mathrm{d}y\,\mathrm{d}x = (\lambda_2 - \lambda_1)(z_0 + A_z)(x_0 + A). \tag{2.8}$$

3. Base solution

The base solution whose stability we will investigate applies for large times far from the endwalls in the x- and z-directions, and is of the following form:

$$\boldsymbol{u} = U(y; Ra, \gamma, \alpha, S)\,\boldsymbol{e}_x, \tag{3.1}$$

$$\theta = \Theta(x, y, t; Ra, \gamma, \alpha, S) = f(y; Ra, \gamma, \alpha, S) + \frac{\lambda_2 - \lambda_1}{2}\,t + S\xi, \tag{3.2}$$

$$p = P(x, y, t; Ra, \gamma, \alpha, S) = P_0 + Gx + \xi\frac{\lambda_2 - \lambda_1}{2}\,t + \tfrac{1}{2}S\xi^2, \tag{3.3}$$

where $\xi = x\cos\alpha + y\sin\alpha$ is a coordinate in the direction opposite to that of gravity, and the functions U and f are as given in SK (pp. 349–352). For non-equal fluxes,

the solution can only be valid for intermediate times, as the linear growth term will eventually cause the underlying assumptions (constant properties etc.) to break down. For some purposes, it is convenient to write

$$\Theta(x, y, t) = g(y) + \frac{\lambda_2 - \lambda_1}{2} t + S_x x; \tag{3.4}$$

this rewriting is in fact necessary for the horizontal case. The integral conditions (2.7) and (2.8) determine the constants G (reduced pressure gradient), and S (stratification) with a relative error $O(\delta_z/A_z)$, where δ_z is a characteristic size of the regions near the z walls where the interior solution is not valid. It turns out that G can be expressed in terms of S, and the latter be found from a transcendental equation of the form

$$F(S, Ra, \gamma, \alpha) = 0. \tag{3.5}$$

The Prandtl number, Pr, does not enter the base solution, because the flow is unidirectional. However, it should be borne in mind that the growth of the thermal and viscous boundary layers begins in the turning regions and that their growth rates are certainly different in high and low Prandtl number fluids, regardless of whether the temperature or heat flux is specified at the walls; this fact, however, does not affect the analysis presented herein. The aspect ratios A and A_z do not enter either as long as they are much larger than the boundary-layer thickness, which is guaranteed *a priori* if $A, A_z \gg 1$. The parameters which determine the base solution are thus Ra, γ, and α. However, in the stability analysis, the Prandtl number, Pr, will also enter, as well as two different wavenumbers. Because of the large number of parameters, we have only made calculations for the case of equal fluxes, $\gamma = 45°$. $S(Ra, \alpha, \gamma = 45°)$ is plotted in figure 2. Solutions with positive S have a natural stratification (heavier at the bottom), whereas $S < 0$ means that the stratification is unnatural.

Before we go on to derive perturbation equations, some further characteristics of the base solution are perhaps worth mentioning. For high Rayleigh numbers and natural stratification, the cross-sectional profiles $U(y)$ and $f(y)$ have boundary layers which both have a typical thickness of $\beta^{-1} = (RaS\cos^2\alpha/4)^{-1/4}$. For vertical orientation, $\cos\alpha = 0$, and $S \approx 0.463Ra^{-1/9}$, which gives $\beta^{-1} \propto Ra^{-2/9}$. The fact that the velocity and temperature boundary layers are of equal thickness, irrespective of Pr, is in sharp contrast to the free convection occurring at a heated, vertical, plate with no stratification in the surrounding fluid, where two different Pr-dependent boundary-layer structures occur, depending on whether $Pr \gg 1$ or $Pr \ll 1$ (Bejan 1984, chapter 2; Leal 1992, chapter 11).

4. Perturbation equations

4.1. *Derivation*

Let

$$\boldsymbol{u} = \{U(y) + \hat{u}\}\,\boldsymbol{e}_x + \hat{v}\,\boldsymbol{e}_y + \hat{w}\,\boldsymbol{e}_z, \tag{4.1}$$

$$p = P(x, y, t) + \hat{p}, \tag{4.2}$$

$$\theta = \Theta(x, y, t) + \hat{\theta}, \tag{4.3}$$

where all the perturbations (marked with hats) are functions of x, y, z, and t, which have small enough amplitudes so that the following linearized equations are

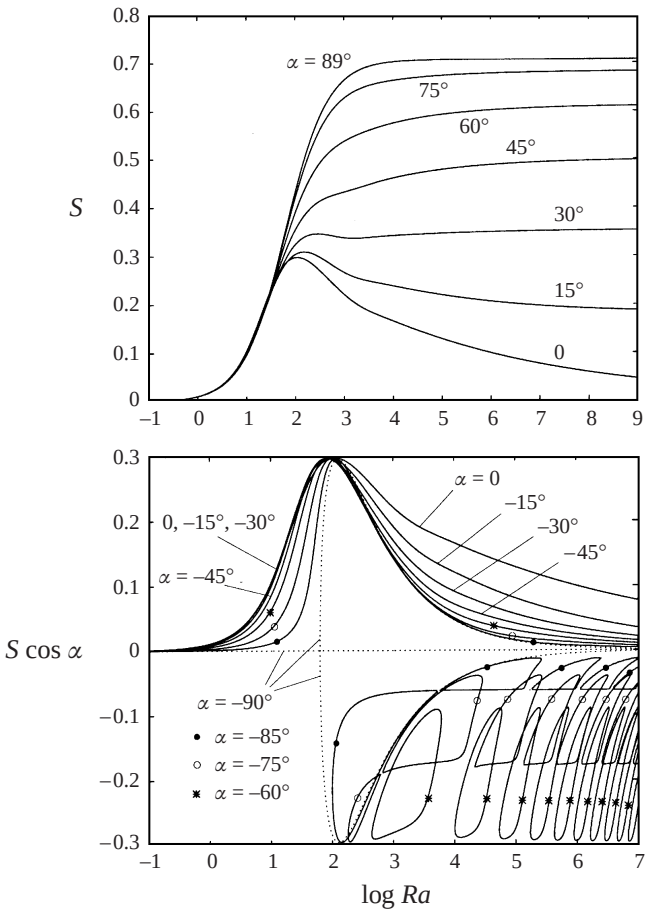

FIGURE 2. Stratification in the base solution for $\gamma = 45°$, from Sundström & Kimura (1996).

approximately valid:

$$\frac{1}{Pr}\left(\frac{\partial \hat{u}}{\partial t} + RaU\frac{\partial \hat{u}}{\partial x} + Ra\hat{v}\frac{\partial U}{\partial y}\right) + \frac{\partial \hat{p}}{\partial x} - \nabla^2\hat{u} - \hat{\theta}\cos\alpha = 0, \tag{4.4}$$

$$\frac{1}{Pr}\left(\frac{\partial \hat{v}}{\partial t} + RaU\frac{\partial \hat{v}}{\partial x}\right) + \frac{\partial \hat{p}}{\partial y} - \nabla^2\hat{v} - \hat{\theta}\sin\alpha = 0, \tag{4.5}$$

$$\frac{1}{Pr}\left(\frac{\partial \hat{w}}{\partial t} + RaU\frac{\partial \hat{w}}{\partial x}\right) + \frac{\partial \hat{p}}{\partial z} - \nabla^2\hat{w} = 0, \tag{4.6}$$

$$\frac{\partial \hat{u}}{\partial x} + \frac{\partial \hat{v}}{\partial y} + \frac{\partial \hat{w}}{\partial z} = 0, \tag{4.7}$$

$$\frac{\partial \hat{\theta}}{\partial t} + RaU\frac{\partial \hat{\theta}}{\partial x} + Ra\hat{u}\frac{\partial \Theta}{\partial x} + Ra\hat{v}\frac{\partial \Theta}{\partial y} - \nabla^2\hat{\theta} = 0. \tag{4.8}$$

On the walls at $y = \pm 1$, the boundary conditions are

$$\frac{\partial \hat{\theta}}{\partial y} = \hat{u} = \hat{v} = \hat{w} = 0. \tag{4.9a–d}$$

The importance of the linearized integral conditions is far from obvious at this point, but let us write them down to facilitate later discussion:

$$\int_{-A_z}^{z_0}\int_{-1}^{1}\hat{u}(x_0,y,z)\,\mathrm{d}y\,\mathrm{d}z+\int_{-A}^{x_0}\int_{-1}^{1}\hat{w}(x,y,z_0)\,\mathrm{d}y\,\mathrm{d}x=0, \tag{4.10}$$

$$\int_{-A}^{x_0}\int_{-A_z}^{z_0}\int_{-1}^{1}\frac{\partial\hat{\theta}}{\partial t}\,\mathrm{d}y\,\mathrm{d}z\,\mathrm{d}x+\int_{-A_z}^{z_0}\int_{-1}^{1}\left(Ra\hat{u}\Theta+RaU\hat{\theta}-\frac{\partial\hat{\theta}}{\partial x}\right)_{x=x_0}\mathrm{d}y\,\mathrm{d}z$$
$$+\int_{-A}^{x_0}\int_{-1}^{1}\left(Ra\hat{w}\Theta-\frac{\partial\hat{\theta}}{\partial z}\right)_{z=z_0}\mathrm{d}y\,\mathrm{d}x=0. \tag{4.11}$$

The coefficients in (4.4)–(4.9) do not depend on x, z, or t. It is therefore possible to find elementary solutions of the form

$$\hat{\phi}=\tilde{\phi}(y)\exp(\sigma t+\mathrm{i}kx+\mathrm{i}mz), \tag{4.12}$$

where ϕ stands for any of the variables u, v, w, p, or θ. The perturbations thus obtained are complex-valued. Rather than directly taking the real part, as is frequently done, let us for the moment be content with having complex solutions, defined in the whole (k,m)-plane, and return later to the task of combining those to obtain real-valued quantities. The applicability of the integral conditions (4.10) and (4.11) is another question that we shall return to later. The ansatz (4.12) leads to the following eigensystem:

$$Pr^{-1}(\sigma+RaU\mathrm{i}k)\tilde{u}+Pr^{-1}Ra\tilde{v}U'-\tilde{u}''+(k^2+m^2)\tilde{u}+\mathrm{i}k\tilde{p}-\tilde{\theta}\cos\alpha=0, \tag{4.13}$$

$$Pr^{-1}(\sigma+RaU\mathrm{i}k)\tilde{v}-\tilde{v}''+(k^2+m^2)\tilde{v}+\tilde{p}'-\tilde{\theta}\sin\alpha=0, \tag{4.14}$$

$$Pr^{-1}(\sigma+RaU\mathrm{i}k)\tilde{w}-\tilde{w}''+(k^2+m^2)\tilde{w}+\mathrm{i}m\tilde{p}=0, \tag{4.15}$$

$$\mathrm{i}k\tilde{u}+\mathrm{i}m\tilde{w}+\tilde{v}'=0, \tag{4.16}$$

$$(\sigma+RaU\mathrm{i}k)\tilde{\theta}-\tilde{\theta}''+(k^2+m^2)\tilde{\theta}+Ra\tilde{u}S_x+Ra\tilde{v}g'=0, \tag{4.17}$$

with the boundary conditions

$$\tilde{u}(\pm1)=\tilde{v}(\pm1)=\tilde{w}(\pm1)=\tilde{\theta}'(\pm1)=0. \tag{4.18a–d}$$

In the numerical treatment we have used, it pays to reduce the number of variables at the cost of increasing the order of the system. Thus, we proceed by eliminating the pressure between equations (4.13) and (4.15). In doing so, the quantity

$$\tilde{\omega}_y=\mathrm{i}(m\tilde{u}-k\tilde{w}), \tag{4.19}$$

which is the amplitude function for the vorticity in the y-direction, naturally appears. The definition (4.19) together with the continuity equation (4.16) makes it possible to express both $\tilde{u}$ and $\tilde{w}$ in terms of $\tilde{\omega}_y$ and $\tilde{v}$:

$$\tilde{u}=\mathrm{i}\left(\frac{k\tilde{v}'-m\tilde{\omega}_y}{k^2+m^2}\right),\quad \tilde{w}=\mathrm{i}\left(\frac{m\tilde{v}'+k\tilde{\omega}_y}{k^2+m^2}\right), \tag{4.20a, b}$$

which is valid whenever at least one of the wavenumbers is non-zero. The case $k=m=0$ is treated in Appendix A. The remaining pressure term $\tilde{p}'$, appearing in equation (4.14), is eliminated by multiplying that equation with k^2+m^2 and adding the derivative of the linear combination $\mathrm{i}k(4.13)+\mathrm{i}m(4.15)$. The perturbation equations

can then be written

$$\frac{\sigma}{Pr}\{q\tilde{v}-\tilde{v}''\}=-\tilde{v}''''+\left(2q+\frac{Raik}{Pr}U\right)\tilde{v}''-\frac{Raik}{Pr}U''\tilde{v}-q\left(q+\frac{Raik}{Pr}U\right)\tilde{v}$$
$$+\mathrm{i}k\cos\alpha\,\tilde{\theta}'+q\sin\alpha\,\tilde{\theta} \qquad (4.21)$$

$$\frac{\sigma}{Pr}\tilde{\omega}_y=\tilde{\omega}_y''-\left(q+\frac{Raik}{Pr}U\right)\tilde{\omega}_y-\frac{Raim}{Pr}U'\tilde{v}+\mathrm{i}m\cos\alpha\,\tilde{\theta} \qquad (4.22)$$

$$\sigma\tilde{\theta}=\tilde{\theta}''-(q+RaikU)\,\tilde{\theta}-\frac{Raik}{q}S_x\tilde{v}'-Rag'\tilde{v}+\frac{Raim}{q}S_x\tilde{\omega}_y, \qquad (4.23)$$

where $q=k^2+m^2$. With the introduction of $\tilde{\omega}_y$, the boundary conditions have transformed to

$$\tilde{v}(\pm1)=\tilde{v}'(\pm1)=\tilde{\omega}_y(\pm1)=\tilde{\theta}'(\pm1)=0. \qquad (4.24a\text{–}d)$$

4.2. *Some mathematical aspects*

For the case $m=0$, (4.22) decouples from (4.21) and (4.23). This means that there are two different eigenvalue spectra: one from (4.21) and (4.23), which gives all solutions with $(\tilde{v},\tilde{\theta})\neq0$, the other from (4.22), which gives all solutions with $\tilde{\omega}_y\neq0$. However, on multiplying (4.22) by the complex conjugate $\tilde{\omega}_y^*$, integrating from $y=-1$ to $y=1$, and taking the real part of that integral, one obtains

$$\frac{\mathrm{Re}\{\sigma\}}{Pr}\int_{-1}^{1}|\tilde{\omega}_y|^2\,\mathrm{d}y=-\int_{-1}^{1}\left(|\tilde{\omega}_y'|^2+k^2|\tilde{\omega}_y|^2\right)\mathrm{d}y \qquad (4.25)$$

which, since both the integrals are positive whenever $\tilde{\omega}_y\not\equiv0$, shows that all such modes will have $\mathrm{Re}\{\sigma\}<0$, and thus be decaying. This means that (4.22) need not be considered when $m=0$. For the different special case $k=0$, the system remains fully coupled.

For the case of equal fluxes, U and g are odd in y. One can then show that if $[\sigma,\tilde{\theta}(y),\tilde{v}(y),\tilde{\omega}_y(y)]$ is a solution, then so is $[\sigma^*,\tilde{\theta}^*(-y),\tilde{v}^*(-y),-\tilde{\omega}_y^*(-y)]$. Since any complex roots occur in conjugate pairs, the characteristic equation can be written in real form, which indicates that one may be able to find an equivalent eigensystem with real coefficients. However, we chose instead to solve the complex system directly.

Since the eigenvalue problem under consideration is not self-adjoint, one may raise the question as to whether or not the eigenfunctions $\tilde{\phi}(y)$ form a complete basis which spans the space of allowed (sufficiently regular) initial conditions. DiPrima & Habetler (1969) have shown a completeness theorem for a class of generalized eigenvalue problems which includes both the two-dimensional Orr–Sommerfeld equation, and a Bénard type problem with bottom heating. It would therefore not be surprising if a complete basis is obtained in the present case as well. However, we are not aware of any proof of this, and must therefore be content to restrict the study to initial conditions that are spanned by the eigenfunctions which are obtained from the ansatz that we have made.

4.3. *Construction of real-valued solutions*

Although any, or both, of the two wavenumbers may be negative, a closer inspection of the system (4.21)–(4.23) reveals some symmetries, which makes it possible to construct solutions for the whole (k,m)-plane from solutions found in the first quadrant (positive k and m). These symmetries are given in table 1; note specifically that the real part

	$-k$	k
m	$\sigma^*, \tilde{\theta}^*, \tilde{v}^*, -\tilde{\omega}_y^*$	$\sigma, \tilde{\theta}, \tilde{v}, \tilde{\omega}_y$ solved
$-m$	$\sigma^*, \tilde{\theta}^*, \tilde{v}^*, \tilde{\omega}_y^*$	$\sigma, \tilde{\theta}, \tilde{v}, -\tilde{\omega}_y$

TABLE 1. The effect of sign shifts in k and m (* denotes the complex conjugate).

of σ, which gives the growth rate, is independent of the sign of the wavenumbers. From (4.20*a*, *b*), $\tilde{u}$ is seen to have the same symmetries as $\tilde{v}$, whereas $\tilde{w}$ has the same symmetries as $\tilde{\omega}_y$.

From the nature of the base flow, we expect waves to be standing in z, but travelling in x. Indeed, table 1 does admit such solutions. (It also admits travelling waves in z, but not standing waves in x.) Adding solutions from all the four quadrants together with equal weights, one obtains the real-valued perturbations

$$\hat{\theta} = \mathrm{Re}\{\tilde{\theta}(y)\exp(\sigma t + \mathrm{i}kx)\}\cos mz, \tag{4.26a}$$

$$\hat{u} = \mathrm{Re}\{\tilde{u}(y)\exp(\sigma t + \mathrm{i}kx)\}\cos mz, \tag{4.26b}$$

$$\hat{v} = \mathrm{Re}\{\tilde{v}(y)\exp(\sigma t + \mathrm{i}kx)\}\cos mz, \tag{4.26c}$$

$$\hat{w} = \mathrm{Re}\{\mathrm{i}\tilde{w}(y)\exp(\sigma t + \mathrm{i}kx)\}\sin mz. \tag{4.26d}$$

Note that (4.26) cannot be obtained by just combining real and/or imaginary parts directly in the ansatz (4.12), since such manipulations only make use of one of the two diagonals in table 1. We have chosen the construction (4.26) for the visualizations presented in figures 6–8. However, other linear combinations are also possible – the analysis made here does not give a definite answer to how the different elementary solutions will combine.

4.4. *Integral conditions*

Knowing that there are regions near the x and z walls (say of sizes Δ_x and Δ_z) where (4.26) is not valid, one is led to ask to what extent the integral conditions (4.10) and (4.11) are applicable. It seems that they can give useful information only if a typical value of the integral in question, I, is much larger than the estimated error due to the end regions, ΔI. Assuming the amplitude of the integrand to be ϕ_{max}, one has

$$I \sim \phi_{max}\min(x_0 + A, k^{-1})\min(z_0 + A_z, m^{-1}). \tag{4.27}$$

Estimating the error due to the end regions to be

$$\Delta I \sim \phi_{max}\{\Delta_x \min(z_0 + A_z, m^{-1}) + \Delta_z \min(x_0 + A, k^{-1})\}, \tag{4.28}$$

the condition for applicability, $\Delta I/I \ll 1$, can be written

$$\Delta_x/\min(x_0 + A, k^{-1}) + \Delta_z/\min(z_0 + A_z, m^{-1}) \ll 1. \tag{4.29}$$

For the case $k = m = 0$, (4.29) indicates that the integral conditions should be applied. The case is treated in Appendix A, with a slightly generalized ansatz.

With $k = 0, m \neq 0$ (and $A_z \gg m^{-1}$) the integral conditions apply only if $m\Delta_z \ll 1$. Typically, however, we expect $m\Delta_z \sim m\Delta_y \sim m\min(1, \beta^{-1}) \sim 1$, so that the integral conditions do not apply. Even for the cases treated in Appendices A and B, where we have found instabilities in the limit as $m \to 0$, it appears inappropriate to apply

the integral conditions, as our numerical results show that, in practice, m need not be very small for these instabilities to occur in the vicinity of the analysed cases (an example is given in figure 6*a*).

Having $k \neq 0$ and $m = 0$ (with $A \gg k^{-1}$) gives, in an analogous manner, the applicability condition $k\Delta_x \ll 1$, which also does not hold for any of the modes which turn out to be of interest.

Also, for cases with both wavenumbers being non-zero, the integral conditions are found not to apply.

5. Numerical solution method

5.1. *The eigenvalue problem*

Any eigensystem of ordinary differential equations, such as (4.21)–(4.24), can be approximated with a generalized matrix eigenvalue problem $\boldsymbol{A}\boldsymbol{x} = \sigma\boldsymbol{B}\boldsymbol{x}$ using, for example, a Galerkin method, a finite element method or a finite difference method; here, a finite difference method with variable order of accuracy was developed, and is presented in § 5.4. Typically, we used it with fourth-order accuracy.

Methods for solving the problem $\boldsymbol{A}\boldsymbol{x} = \sigma\boldsymbol{B}\boldsymbol{x}$ include inverse iteration methods, the QZ method, and various methods for solving $\det(\boldsymbol{A} - \sigma\boldsymbol{B})$ directly as a polynomial equation in σ. We chose the QZ method, which is comparatively slow, but finds all the eigenvalues without any initial guess. The method is described in Golub & van Loan (1996), and has been implemented in the LAPACK Fortran subroutine cgegv.f, which we have used. On a CRAY-J90 supercomputer, it typically took 1 s of CPU time to solve the complete eigenvalue problem to desired accuracy.

However, the results we aim for involve solving the eigenvalue problem many times (in fact, we estimate that all the results contained in this paper required of the order of 10^6 solutions), so that even more speed is desired. Rather than trying faster methods for the matrix eigenvalue problem, we applied the method of shooting with fourth-order Runge–Kutta integration to trace out most parts of the criticality curves. The method gives an accurate eigenvalue from an initial guess in about 10^{-2} s on the same computer, and also provides a check that the equations have been typed in correctly. Initial guesses have been taken either from previous points or from the FD/QZ method. Grid sizes have been automatically doubled to give errors which are invisible in the plots. Typically, between 40 and 80 grid points was enough, although it was found to depend on the eigenmode and the parameter region.

In the shooting method, the original equations are first rewritten as a first-order system. That system is then integrated from the left to the right boundary. To be able to do this integration, both σ and the values at the left boundary of $\tilde{\theta}$, $\tilde{\omega}_y'$, $\tilde{v}''$, and $\tilde{v}'''$, are needed. One of the latter (we chose $\tilde{\theta}$) can be fixed, as the amplitude would otherwise be undetermined. The remaining four values are then solved for, using a multidimensional Newton method, from the requirement that all the four boundary conditions at the right boundary be fulfilled.

5.2. *Criticality conditions*

If we denote the eigenvalue with the largest real part by σ_r, the criticality conditions are defined through

$$\max_{k,m} \sigma_r(Ra, k, m, \gamma, \alpha, Pr) = 0, \tag{5.1}$$

which leads to the following system of equations:

$$\left.\begin{aligned} \sigma_r(Ra, k_c, m_c, \gamma, \alpha, Pr) &= 0, \\ \frac{\partial \sigma_r}{\partial k}(Ra, k_c, m_c, \gamma, \alpha, Pr) &= 0, \quad \text{or } k_c = 0, \\ \frac{\partial \sigma_r}{\partial m}(Ra, k_c, m_c, \gamma, \alpha, Pr) &= 0, \quad \text{or } m_c = 0. \end{aligned}\right\} \tag{5.2}$$

In solving this, three of the parameters Ra, γ, α, and Pr are held fixed, and the fourth is varied to fulfil the equations. We chose Ra as the critical parameter, except on parts of the criticality curves with large values of $\mathrm{d}(Ra)/\mathrm{d}\alpha$, where α was solved for instead. Regarding the above as a system of the type $f_j(x_k) = 0$, it can be solved using a multidimensional Newton method,

$$0 = f_j^{(i)} + \sum_k \frac{\partial f_j^{(i)}}{\partial x_k}(x_k^{(i+1)} - x_k^{(i)}), \tag{5.3}$$

where the superscript i denotes values at the ith iteration. All the derivatives appearing in both the functions and the Jacobian are evaluated numerically. Most calculations were made on a CRAY-J90, and could be parallelized in a simple way: the heavy part in evaluating the functions and the Jacobian in (5.3) is just a number of independent evaluations of σ_r, which are conveniently assigned to different processors. Initial guesses were obtained from nearby points in the parameter space and the system iterated until a convergence criterion was satisfied for a few consecutive iterates. Evaluations of σ_r over the (k, m)-plane were made at some points to detect the possible appearance of more unstable branches.

5.3. *Some difficulties and their remedies*

For cases with extremely thin boundary layers, a special treatment, presented in Appendix C, was found to be necessary in order to maintain good accuracy for a reasonable effort.

In some cases (boundary-layer cases when still the whole region was solved for), the Runge–Kutta integration diverged even from a guess which was good enough to make the eigenfunctions near $y = -1$ indistinguishable on a plot. These problematic cases were solved directly with the QZ method.

Even the QZ method failed to converge in one of the parameter regions. The problems occurred for modes with $k = 0$ in cases with boundary layers when the whole region was solved for. The source of the problem turned out to be a degeneracy in the system, the two most unstable eigenvalues being almost identical when $\lambda_1 = \lambda_2$. With $k = 0$, all the coefficient functions which remain in the system are symmetric in y, and all the derivatives of the perturbations are even (symmetry-preserving). If an arbitrary eigenmode is split into its odd and even parts, use of the symmetries shows that these parts are uncoupled. Solving the odd and even eigenfunctions separately, the convergence problems could be eliminated, and the computations carried out more cheaply (the QZ method requires $O(n^3)$ floating point operations, where n is the order of the matrices, and $2(n/2)^3 < n^3$). Both problems were solved on the interval $[-1, 0]$. In order to separate the odd and even modes, the following boundary conditions were applied at $y = 0$:

$$\left.\begin{aligned} &\text{odd modes:} \quad \tilde{v} = \tilde{v}'' = \tilde{\omega}_y = \tilde{\theta} = 0; \\ &\text{even modes:} \quad \tilde{v}' = \tilde{v}''' = \tilde{\omega}_y' = \tilde{\theta}' = 0. \end{aligned}\right\} \tag{5.4}$$

5.4. *The finite difference method with variable order of accuracy*

The discretization is obtained by including the calculation of the coefficients in the differencing molecules as part of the code. In deriving a discrete approximation of order n for a derivative of order d at a grid point y_i, we first use Taylor's formula to express the known values at the neighbouring points y_j in terms of the unknown derivatives at y_i:

$$\phi_j - \phi_i = \sum_{k=1}^{N} \left.\frac{\partial^k \phi}{\partial y^k}\right|_{y_i} \frac{(y_j - y_i)^k}{k!} + O((y_j - y_i)^{N+1}). \tag{5.5}$$

To isolate the dth derivative, the terms with lower derivatives from 1 to $d-1$ must be eliminated, and to obtain nth-order accuracy, the terms with higher derivatives from $d+1$ to $d+n-1$ must also be eliminated. This adds up to $d+n-2$ terms, whose elimination requires $d+n-1$ equations. Thus, we set $N = d+n-1$ in (5.5) and evaluate it at $d+n-1$ different points y_j (as centred as possible around y_i). We obtain

$$\sum_{k=1}^{d+n-1} A_{jk} \left.\frac{\partial^k \phi}{\partial y^k}\right|_{y_i} = (\phi_j - \phi_i) + O((y_j - y_i)^{d+n}), \text{ where } A_{jk} = \frac{(y_j - y_i)^k}{k!}. \tag{5.6}$$

A_{jk} (whose dependence on i has been suppressed for clarity) can be seen as elements in a matrix $\boldsymbol{A}$, which can be inverted to give

$$\left.\frac{\partial^k \phi}{\partial y^k}\right|_{y_i} = \sum_j (\boldsymbol{A}^{-1})_{kj}(\phi_j - \phi_i) + O((\Delta y)^{d+n-k}), \tag{5.7}$$

where Δy in the error estimate is a typical grid spacing within the differencing molecule, and the $-k$ in the exponent comes from the kth column of $\boldsymbol{A}$ being $O((\Delta y)^k)$ – with the limited aim of investigating how the error scales with the grid spacing it is permissible to assume $k! \sim O(1)$. Equation (5.7) shows that the coefficient for ϕ_j where $j \neq i$ can be found in the dth row, jth column of the matrix $\boldsymbol{A}^{-1}$. The coefficient for ϕ_i is then obtained as minus the sum of the other coefficients. The time taken to calculate all the needed discretizations by inverting the various small matrices resulting from the above procedure is, cumbersome as it may seem, actually negligible compared to the time for solving the matrix eigenvalue problem. The procedure to evaluate derivatives away from grid points is very similar, and actually even simpler since all the grid points involved are equivalent for that case.

Finally, the grid must be chosen. That is, for each variable one must determine both a set of definition points, y_j, at which the discrete variable is defined, and a set of evaluation points, y_e, at which the corresponding equation is evaluated. (This way of looking at it is a generalization of the ideas we have encountered in the literature.) To keep the differencing molecules symmetric over the whole interval, and thereby avoid the Runge phenomenon (Dahlquist, Björck & Anderson 1974), some definition points are placed outside the boundary, the number of such points for each variable being equal to half the width of the largest differencing molecule for that variable. With this construction, there are more points outside the domain than there are boundary conditions to eliminate them; therefore, a number of extra evaluation points are inserted between definition points near the boundaries, as shown in figure 3. Boundary-layer cases were treated with grids having a certain fraction of the total number of grid points uniformly distributed within the boundary layer, and the remaining points in an expansion factor grid in the interior, whose expansion

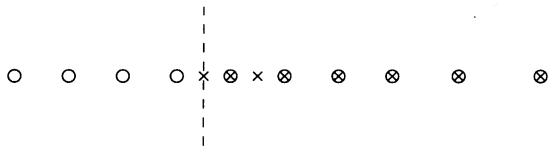

FIGURE 3. Sample grid for the finite difference method (gives fourth-order accuracy in the $\tilde{v}$-equation); ○ are definition points, where the discrete variable $\tilde{v}_i$ is defined; × are evaluation points, where the $\tilde{v}$-equation is evaluated.

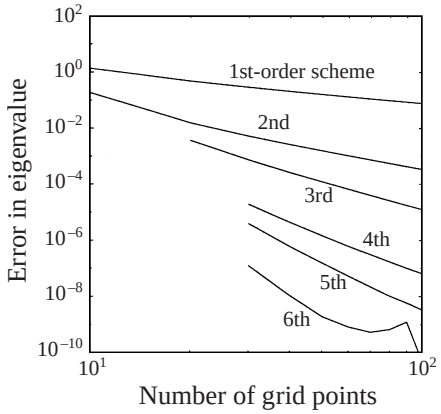

FIGURE 4. Accuracy test for the variable-order FD/QZ method.

factor was solved for, using Newton's method, to make the sum of the cell widths (a geometric series) equal to the interval to be covered. For cases without boundary layers, a uniform grid was used.

Some false eigenmodes were seen to arise. Fortunately, those could be sorted away easily, since they were invariably close to zero in the interior and had large values outside the domain. The number of such modes increases with the order of accuracy.

As a test case, the free–free Bénard problem (Chandrasekhar 1961, II:15, originally due to Lord Rayleigh 1916), was solved at the known critical point. The results, presented in figure 4, indicate that the expected order of accuracy is obtained, up to a limit determined by machine precision.

6. Results

6.1. *Inclined cases, selected Pr*

The criticality conditions in the (Ra, α)-plane, for some selected values of Pr, are presented in figure 5. Colours have been used to code the different Prandtl numbers, whereas the line style gives some information about the destabilizing mode. The parts of the criticality curves where Ra is larger than some value in the range 10^6–10^8 have been calculated using the boundary-layer scaling of Appendix C. Results are typically obtained with at least three significant digits so that errors should be invisible on the plot. The smooth (invisible) joining of the boundary-layer curves to those without that assumption indicates that this is indeed the case. The dotted curves have one dot for each data point, and the density of data points is similar for the other curves.

The Prandtl numbers in the study have been chosen to be characteristic of different materials. Results are presented for $Pr = 0.025$ (mercury), $Pr = 0.1$ (liquid steel),

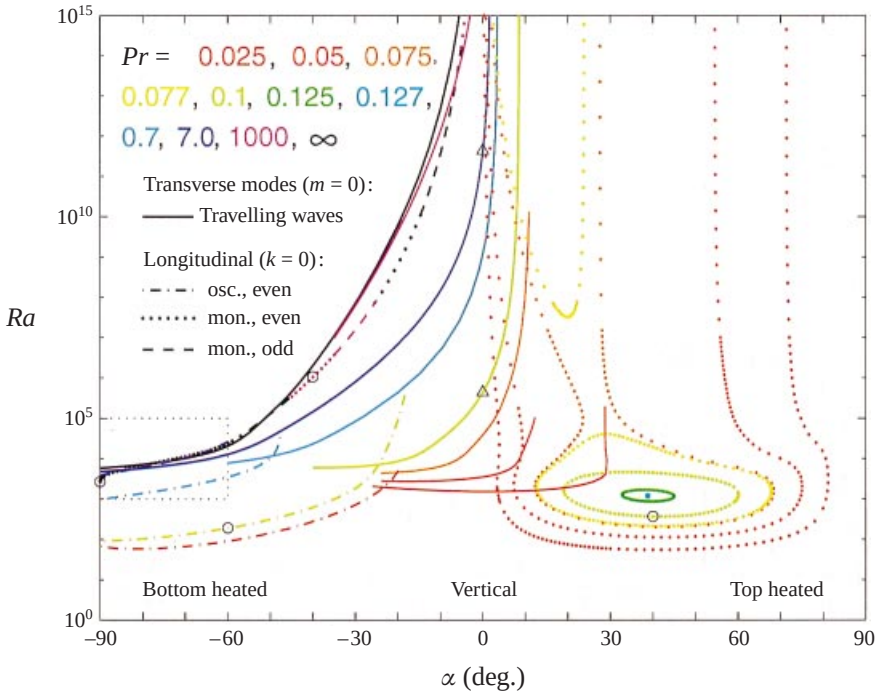

FIGURE 5. Neutral stability curves for the case of equal fluxes and natural stratification ($\gamma = 45°, S > 0$). The region in the dotted rectangle is studied more closely in figure 9, whereas the vertical case is presented more fully in figure 10. Destabilizing modes, at the points marked ◯ and △, are visualized in figures 6 and 7.

$Pr = 0.7$ (air), $Pr = 7$ (water), and $Pr = 1000$ (typical Schmidt number ν/D for ion diffusion in an electrolyte). The remaining curves $Pr = 0.05, 0.075, 0.077$, 0.125, and 0.127, which are not completely presented, are there to facilitate interpolation. They also show how the unstable region on the positive-α side for $Pr = 0.025$ becomes an island of instability for $Pr = 0.1$, which vanishes as Pr is increased beyond 0.127.

Figures 6–8 give a qualitative picture of the different destabilizing modes. In all those figures, the colour indicates the temperature, with a scale from blue (cold) to red (hot). The coloured streamlines in figure 6 represent the perturbation field at $t = 0$. They have been traced out from the frozen velocity field using Heun's second-order method for the time integration and cubic spline interpolation to find the local velocities. For the time integration, a fourth-order Runge–Kutta scheme was also tried, but was found to perform less well. A possible cause is the lack of smoothness in the spline-interpolated velocity field; the issue may be of some general interest for particle tracking in interpolated velocity fields. The streamfunction which is shown in figures 7 and 8 is the ordinary streamfunction for two-dimensional incompressible flow, and was obtained from numerical integration of the u velocities. The arrows on the streamfunction contours show the direction of the flow. Whereas figures 6 and 7 show only the perturbations, figure 8 also gives an example of a superposition of base fields and perturbation.

The mode which causes the instability for positive α is perhaps the most peculiar one. Figure 6(d) may give the impression that the mode transports warm fluid

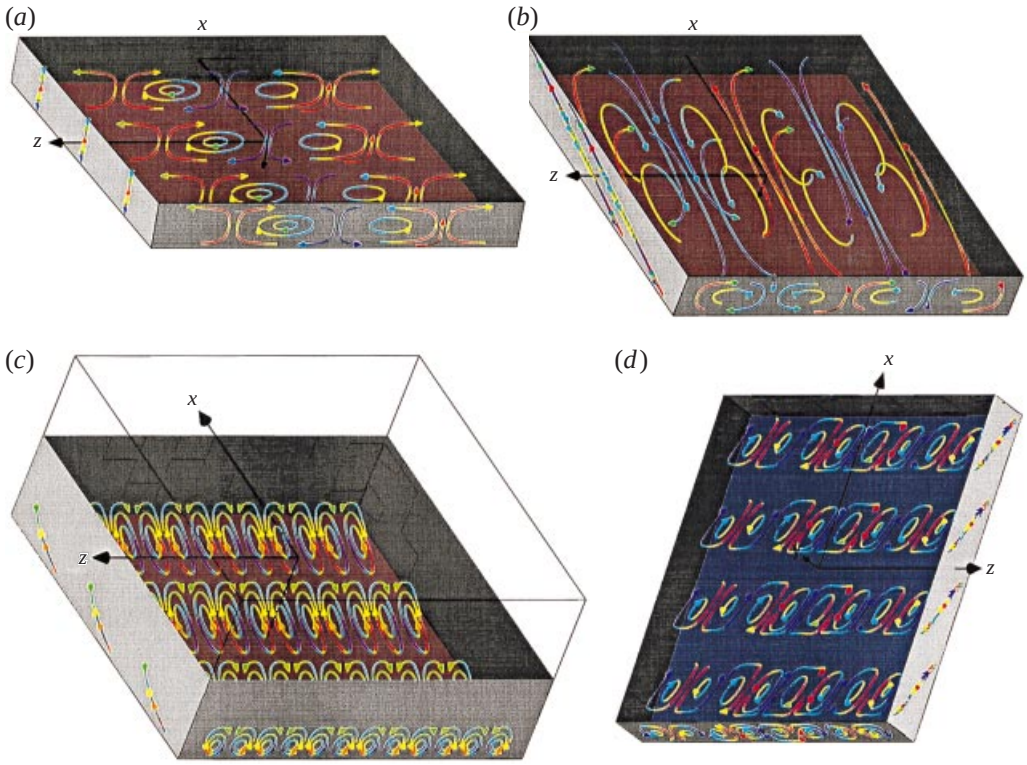

FIGURE 6. Instantaneous streamlines, coloured according to the local temperature, for different longitudinal ($k = 0$) modes at the onset of instability. Only the perturbation fields are shown. (*a*) Monotonic even mode (the subject of Appendix B): $Ra = 2689$, $Pr = \infty$, $\alpha = -89.998°$, $m = 0.683$, $\sigma = 0$. As $\alpha \to 90°$, $m \to 0$ and $Ra \to 2568$. (*b*) Oscillatory even mode (standing wave): $Ra = 195$, $Pr = 0.1$, $\alpha = -60°$, $\sigma = 1.75\mathrm{i}$. (*c*) Monotonic mode with boundary-layer character (a linear combination of an odd and an even mode, which are equally unstable): $Ra = 1.07 \times 10^6$, $Pr = 1000$, $\alpha = -40°$, $m = 10.5$, $\sigma = 0$. (*d*) Monotonic even mode for a case with top heating: $Ra = 375$, $Pr = 0.1$, $\alpha = 40°$, $m = 1.73$, $\sigma = 0$.

away from the cold wall! However, one must not forget the presence of the strong stratification, and, taking the inclination of the streamlines into account, one realizes that the warm fluid in question has its excess heat because it comes from a layer higher up.

6.2. *Comparison with the fixed temperature case*

For comparison, we refer to the experimental observations by Hart (1971) for the constant temperature case, which were found to agree well with the linear stability analysis in the same work (Hart's 1971 figure 6, p. 552). R_a in that figure is a Rayleigh number based on the distance between the plates and the difference in temperature between them, whereas δ is an inclination angle, equal to $-\alpha$. The experiments were made with water ($Pr = 6.7$). Many features are common to our and Hart's results. These include the existence of a region of complete stability near the $\alpha \to 90°$ limit, a region of longitudinal ($k = 0$) instabilities for intermediate, positive, inclination angles, a region near $\alpha = 0$ where transverse ($m = 0$) modes are destabilizing, and a second longitudinal mode region for negative α. However, for the present case, the longitudinal instability for positive α does not occur if Pr is as high as 6.7. Also,

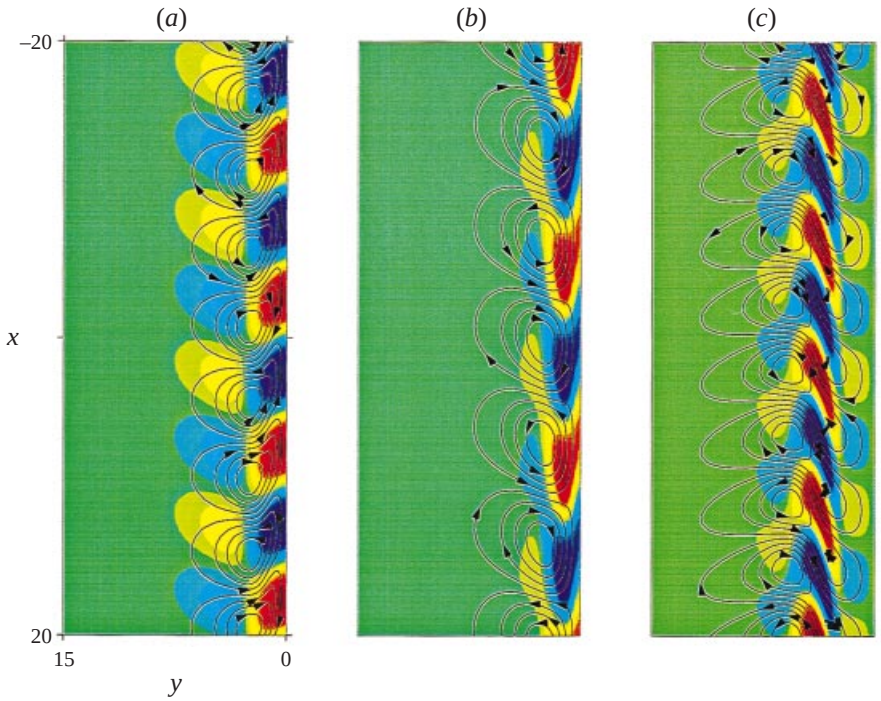

FIGURE 7. Three different travelling-wave boundary-layer modes, which are destabilizing for different Pr in the vertical case. The plots show streamfunction and temperature perturbations near the cooled wall. The (*a*) and (*b*) modes travel downwards, with the base flow, whereas the (*c*) mode travels in the opposite direction. Boundary-layer scaling is used, as described in Appendix C.

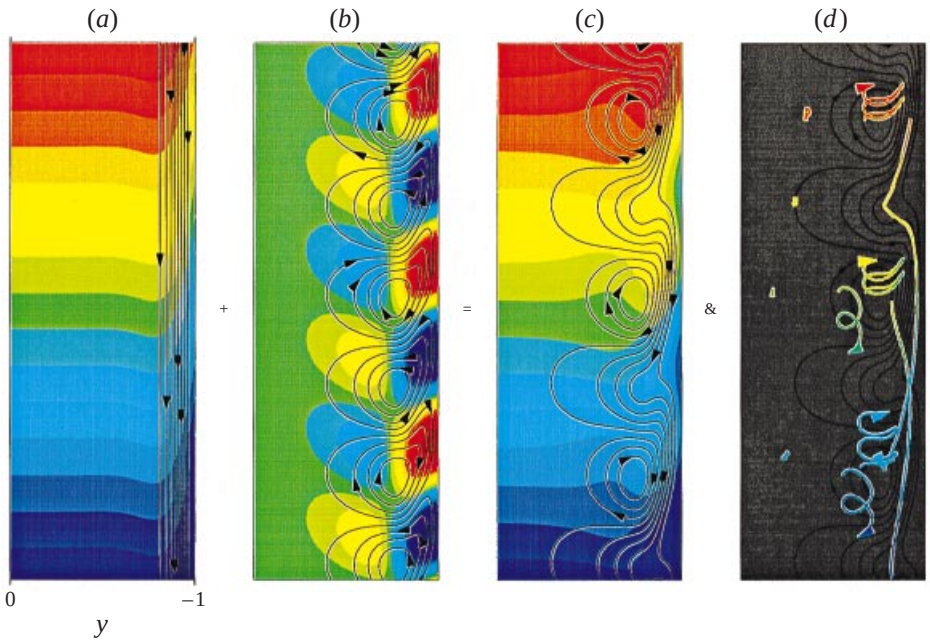

FIGURE 8. A detailed study of a transverse travelling wave. $Ra = 4.4 \times 10^5$, $Pr = 0.1$, $\alpha = 0$, $k = 6.5$, $\sigma = 150\mathrm{i}$. (*a*) Base-solution streamfunction, Ψ, and temperature, Θ. (*b*) Perturbations $\hat{\psi}$ and $\hat{\theta}$ at $t = 0$. The whole pattern moves downwards at constant speed. (*c*) Total ψ and θ at $t = 0$. The perturbation amplitude is (has been arbitrarily chosen to be) about 30% in cross-sectional temperature variation. (*d*) Particle paths during two periods, starting from the flow in (*c*).

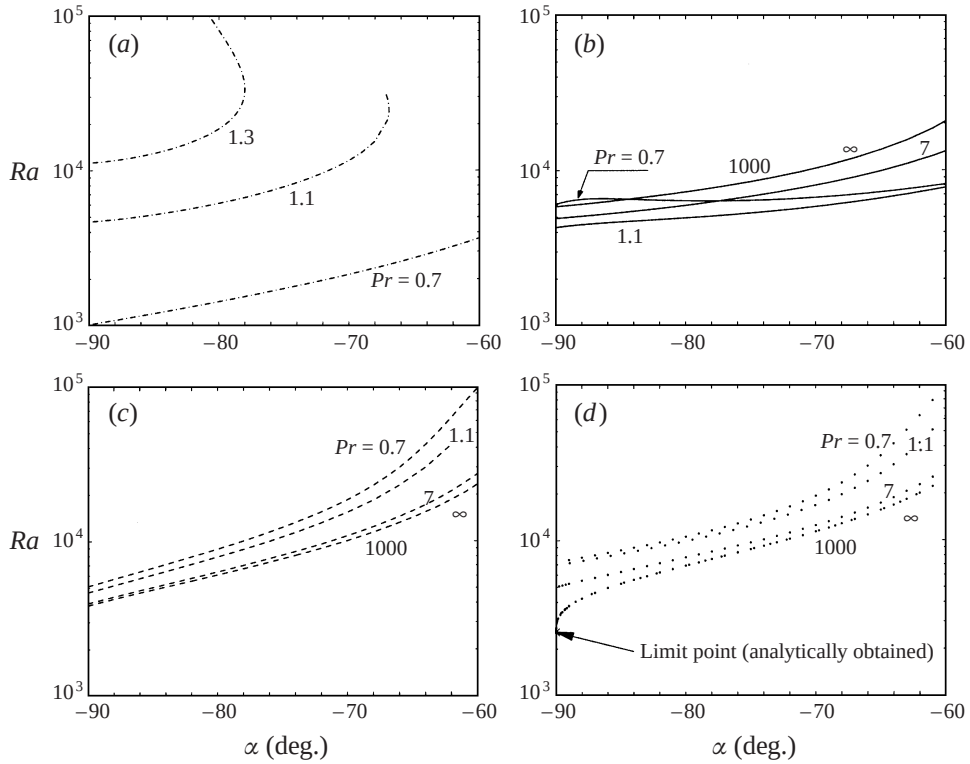

FIGURE 9. Neutral stability curves for four different modes near the bottom-heated limit. (*a*) Oscillatory even longitudinal mode (standing wave). (*b*) Transverse travelling wave. (*c*) Monotonic odd longitudinal mode (roll). (*d*) Monotonic even longitudinal mode (roll).

the stability regions in our case are generally much larger than in Hart's case. This matter is further discussed in § 6.4 on the vertical case.

6.3. *Close-up of the region* $-90^\circ < \alpha < -60^\circ$

For these bottom-heated cases, we have found four different modes to be destabilizing, each for a different range of Pr and α. Figure 9(*a–d*) shows, in separate plots, the criticality conditions for these four modes. The individual modes are as follows:

(*a*) This mode has $k = 0$, $m \neq 0$, is even in y, and gives an oscillatory instability. It is destabilizing in a large-α region for Pr smaller than about 1. As Pr is increased beyond 1, the mode is strongly stabilized, and becomes completely stable for Pr larger than about 1.4. The criticality curves have an upper branch at which an increase in Ra is stabilizing, but, since there are other modes which are unstable on that branch, this should have no practical implications. The mode was not encountered in the case studied by Hart (1971). Figure 6(*b*) shows an instantaneous picture of counter-rotating, strongly inclined, rolls. Half a period later, both temperature and velocity perturbations become reversed.

(*b*) This mode has $k \neq 0$, $m = 0$, and gives an oscillatory instability. As the enclosure is raised from the horizontal, the critical Ra of this mode does not increase as fast as for the other modes, meaning that this mode eventually becomes destabilizing. However, near $\alpha = -90^\circ$, the (*a*) mode tends to be more unstable if Pr is small, whereas the (*c*) and (*d*) modes dominate if Pr is large, although there is a region,

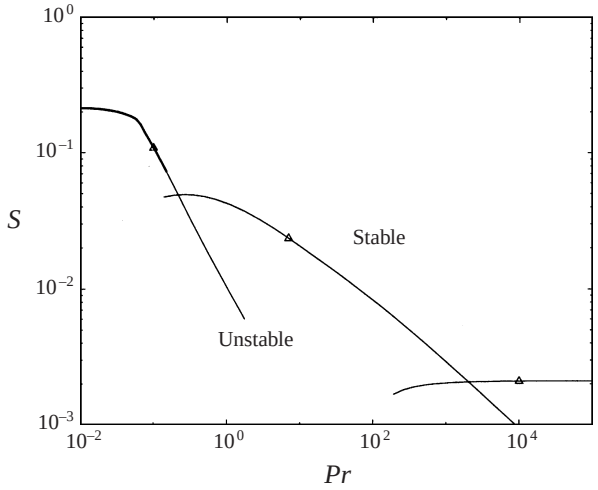

FIGURE 10. Neutral stability curves for the vertical case. The boundary-layer treatment has been used, except for on the thick part of the leftmost curve. Consequently (see Appendix C), the stratification parameter, S, is chosen as the critical parameter. The three different destabilizing modes are studied in figure 7.

near $Pr = 1$, where the (b) mode is destabilizing for all α. The same mode, but for a vertical case in the boundary-layer limit, is visualized in figure 7(b).

(c) This mode has $k = 0$, $m \neq 0$, is odd in y, and gives a monotonic instability. It is important near the horizontal case, if Pr is larger than one. However, for very large Pr, and α very close to $-90°$, its even counterpart, the (d) mode, becomes even more unstable. As the enclosure is raised from the horizontal, one reaches a region in which the base solution has boundary layers. In this region, the growth rates for the (c) and (d) modes are indistinguishable; the boundary-layer mode which is visualized in figure 6(c) can be thought of as a linear combination of the two. The figure shows inclined, counter-rotating rolls, which are elongated in the x-direction.

(d) This mode has $k = 0$, $m \neq 0$, is even in y, and gives a monotonic instability. It is destabilizing only for very large Pr and α less than about $-88°$. For α close to $-90°$, the critical values of Ra and m depend very sensitively on α. At the single point of infinite Pr and $\alpha = -90°$, the numerical solution for Ra_c and m_c fails to converge. Results for finite values of Pr seem to suggest that m_c approaches zero as $Pr \to \infty$, which would explain the problem (since we solve for the logarithm of m_c). To find out what goes on in the limit, some analysis has been done, and is presented in Appendix B. The analysis shows that for $\alpha = -90°$ and $Pr \to \infty$, the critical point is $m_c \to 0$, $Ra_c \to 2568$. This value has been marked with an asterisk in figure 9(d). The perturbation itself is seen in figure 6(a) to be of a simple roll nature, where the rolls become wider as the limit is approached.

6.4. *The vertical case*

Three different modes, all with $k \neq 0$, $m = 0$, and $\mathrm{Im}(\sigma) \neq 0$, are destabilizing in the vertical case, each for a different Prandtl number range. Their stability boundaries are given in figure 10, and the perturbations are visualized in figure 7(a–c). Except for cases with $Pr \ll 1$, there are boundary layers at criticality, which motivates the use of the scaling in Appendix C. With that scaling, S, but not Ra, appears explicitly

in the perturbation equations, and becomes a logical choice as a criticality parameter. As can be seen in figure 10, a larger stratification favours stability.

The corresponding critical Rayleigh numbers (at steady state) are extremely large, up to $O(10^{21})$ for large values of Pr. Expecting such cases to be turbulent, one is led to consider the limitations of the theory. It may be fair to say that *when extrapolating an analysis for infinitesimal disturbances to a reality with finite disturbances, the separation line between the stable and unstable regions becomes one between a possibly stable region and one which is definitely unstable*. That this distinction is important is most clearly seen in a plane Couette flow, which is linearly stable for all Reynolds numbers, but in reality cannot be maintained for large Reynolds numbers, due to transient growth of finite disturbances (Lundbladh & Johansson 1991).

It may still be that even the large-Pr part of figure 10 has some relevance. In transient cases, Bark, Alavyoon & Dahlkild (1992) found the approach to steady state to be such that the boundary layers adjust, almost instantaneously, to a slowly developing stratification. As the time scale for boundary-layer adjustment, β^{-2}, is the same as that for boundary-layer instabilities, there are no further assumptions involved in applying the critical S from figure 10 to transient situations. In doing so, S may be set equal to a value outside the boundary layer of $-\nabla\theta \cdot \boldsymbol{e}_g$, which generally varies with x. The x-location at which instabilities are most likely to occur is that with the smallest value of S. One may expect situations when instabilities of the predicted type exist in the less stratified regions, and are damped out elsewhere.

To enable comparison with a well-established result (Gill & Davey 1969; Bergholz 1978), the boundary condition on the temperature fluctuation at the wall was temporarily changed to $\tilde{T} = 0$. For $Pr = 10$, critical S was found to be 1.664×10^{-2}. This is to be compared with $\sqrt{2}/(\hat{R}_c Pr)$, where $\hat{R}_c$ in the notation of Bergholz (1978) is the critical value of a Reynolds number for the boundary layer, found to be 8.50 for $Pr = 10$, so that we should have $S_c = \sqrt{2}/85.0 = 1.66(38) \times 10^{-2}$, which indeed was obtained. This result, together with the agreement between the numerical results and the analytical ones of Appendices A and B, the agreement between the FD/QZ and RK methods, the qualitative similarities with the constant temperature case (Hart 1971), and a check of the perturbation equations versus those of Hart (1971), constitute the verification.

Changing the boundary condition back to $\tilde{T}'(0) = 0$, one obtains $S_c = 2.062 \times 10^{-2}$ (slightly more unstable). We conclude that it is not the different boundary condition on the perturbation which makes the constant flux case much more stable than the constant temperature case. Instead, the reason must be found in the base solution, where the only difference is that the constant flux case has a much larger stratification. This in turn reduces both the amplitude and the boundary-layer thickness of both the velocity and temperature profiles, which explains the strong tendency for stability.

For completeness, let us briefly discuss some modes which are not destabilizing. In Bergholz (1978), where the stratification was varied as a free parameter, monotonically growing transverse rolls with their axis in the z-direction, extending over the whole interval $y \in [-1, 1]$, were found to be destabilizing in some parameter regions. In our case, with the stratification determined as part of the base solution, such rolls were found too – but only among the damped eigenmodes. A work by Le Quéré & Pécheux (1989) may deepen our understanding. They studied an air-filled gap between two concentric vertical cylinders with fixed temperatures. For low Ra they found a conduction-dominated solution. Increasing Ra they observed a first transition to rolls, a second more gradual one to unicellular boundary-layer flow, and a third to a state with travelling waves. In the second transition, the rolls disappeared one by

one as the stratification increased. In the present case, it seems that the stratification becomes important at an Ra which is too low to give the roll instability a chance to set in. Modes which one may classify as internal waves were also found among the damped eigenmodes. This appears to be the case also when the wall temperatures are prescribed, but is evidently not true for transient flows, in which they are known to appear (Patterson & Imberger 1980; Le Quéré & Pécheux 1989).

7. Concluding remarks

For the case of equal fluxes, it has been shown in which regions of the (Ra, α, Pr) parameter space the unicellular base solution from Sundström & Kimura (1996) is stable to infinitesimal perturbations. Figure 5 summarizes the results. The uniform flux case is found to be much more stable than that of Hart (1971) with fixed wall temperatures, a fact which is attributed to the much larger stratification which occurs in the base solution. As could be expected, instabilities tend to be favoured by a decrease in Pr, an increase in Ra, and a decrease in α; however, exceptions to all these rules could be found.

Cases in which the wavenumber is zero, or approaches zero in different ways, are studied analytically. Integral conditions, derived from the unresolved end regions, are applied in the analysis. The results show that all the base solutions with unnatural (top heavy) stratification are unstable to large-wavelength stationary rolls whose axes are parallel with the base flow.

We conclude by suggesting some further developments.

Variation of γ. In many electrochemical systems, the mass fluxes of ions at the two walls are not equal, so that one would need to use different values of the parameter γ.

End region boundary layers. It would be of some interest to investigate the stability of the boundary layers on the endwalls at $x = \pm A$, at least those for positive α, for which a simple analytical solution is given in SK.

The eigensystem. A closer investigation would be needed to verify, or falsify, our numerical indications that the destabilizing modes must be either longitudinal or transverse, as well as our assumption that the eigenfunctions obtained constitute a complete basis in which any physically possible initial condition can be expanded.

Morphological instabilities. These are instabilities in surface shape, which may be regarded as the initial stages of dendrite formation. This is known to occur both during the solidification of a melt (Davis 1990), and in electrochemical metal refining (Sundström & Bark 1995).

Algebraic growth. Studies on such phenomena are a useful, if not necessary, complement to any stability analysis in which the eigenmodes are non-orthogonal, which is the case here. Because of cancellation in the eigenmode expansion of the initial conditions, even a sum of decaying eigenmodes can grow initially, and may even reach the nonlinear region, in which case the linear solution breaks down and its predicted decay for large times never occurs. Some theory and further references are given in Reddy & Henningson (1993).

Energy stability. To determine a parameter region in which the base solution is definitely stable, one can find the criteria for no initial growth of any perturbation, often referred to as energy stability criteria (Joseph 1976, chap. VIII, 56, 57).

Finite aspect ratios. To investigate the effect of finite aspect ratios, one would presumably need to do some experimental work, or numerical simulations of unsteady three-dimensional cases. Such work may also clarify to what extent our construction of real-valued perturbations agrees with what is actually observed.

Secondary instabilities. Naturally, even the flow that arises beyond the stability boundary may lose its stability. The complexity of the secondary stability problem depends entirely on the structure of the new base solution, which will be different for different modes. In general, a fast and accurate three-dimensional numerical code would be needed. Although very little has been done in this regard, papers by Chait & Korpela (1989) and Wang & Korpela (1992) have studied the secondary instabilities that arise in problems closely related to the one presented here; in particular, they find that secondary instabilities set in rather close to the primary instability boundary via the mechanism of subharmonic resonance, a feature that is typical of inflectional velocity profiles. Also of significance here are the computations of Le Quéré & Pécheux (1989) and Le Quéré (1990*a,b*), which use spectral methods and are thus the most reliable of those that address the boundary-layer regime; structures are found that are similar those in the present paper, as well as indications as to how the instability propagates through the end regions, a feature that a linear stability analysis in an infinite domain cannot address.

The numerical method. It would be of interest to test the variable-order finite difference method developed here, primarily against the Galerkin method, using either Chebyshev polynomials or some problem-dependent basis functions. Having made all the improvements we could think of, we believe that the method is already close to optimal as compared to other finite difference approaches, and possibly finite element approaches as well, as those tend to give similar discrete equations. However, it would be necessary to run extensive tests to verify, or falsify, this belief.

The authors wish to thank Dr Gustav Amberg and Professor Fritz Bark at the department of Mechanics, KTH, for fruitful discussions, Dr Kamen Kanev, Tohoku National Industrial Research Institute, Sendai, Japan (presently at the Visual Science Laboratory in Tokyo), for valuable programming advice, and Professor Shigeo Kimura at the same organization (presently at Kanazawa University), for hosting the first author's visit to Sendai in late 1995, when the work was initiated. In addition, we thank the referees for their comments on an earlier version of the paper. Financial support from the Swedish Research Council for Engineering Sciences (TFR) and a travel grant from the Blanceflor Foundation has made the work possible.

Appendix A. The cases $k = m = 0$, $k \to 0, m = 0$, and $k = 0, m \to 0$

When $k = m = 0$, the original ansatz for the pressure perturbation can be generalized somewhat to

$$\hat{p} = (\tilde{p}(y) + ax + cz)\mathrm{e}^{\sigma t}, \tag{A 1}$$

where a and c are constants (if only one of the wavenumbers is zero, no similar generalization can be made).

Consider the system of equations (4.13)–(4.17). The continuity equation (4.16), unaffected by the change in the pressure ansatz, gives $\tilde{v}' = 0$ which, together with the boundary conditions for $\tilde{v}$, gives $\tilde{v}(y) \equiv 0$. The remaining equations become, with the new pressure,

$$\frac{\sigma}{Pr}\tilde{u} - \tilde{u}'' + a - \tilde{\theta}\cos\alpha = 0, \tag{A 2}$$

$$\frac{\sigma}{Pr}\tilde{w} - \tilde{w}'' + c = 0, \tag{A 3}$$

$$\sigma\tilde{\theta} - \tilde{\theta}'' + Ra\tilde{u}S_x = 0, \tag{A 4}$$

with the boundary conditions

$$\tilde{u}(\pm 1) = \tilde{w}(\pm 1) = \tilde{\theta}'(\pm 1) = 0. \qquad (A\,5a\text{–}f)$$

Since all the coefficients are symmetric in y (in fact, independent of y) and there are only even derivatives of the perturbations, there will be one even and one odd family of solutions.

For this case, there is, except for an arbitrariness in time shift and amplitude, only one way to construct real-valued solutions, namely $\hat{\phi} = \mathrm{Re}\{\tilde{\phi}\,\exp(\sigma t)\}$.

Requiring the integral condition (4.10) to hold for any x_0 and z_0 gives the two conditions

$$\int_{-1}^{1} \tilde{u}\,\mathrm{d}y = 0, \quad \int_{-1}^{1} \tilde{w}\,\mathrm{d}y = 0. \qquad (A\,6a,b)$$

From (4.11) one obtains, with the aid of (A 6a) and (A 4)

$$\int_{-1}^{1} (\tilde{u}\Theta + U\tilde{\theta})\,\mathrm{d}y = 0, \quad \int_{-1}^{1} \tilde{w}\Theta\,\mathrm{d}y = 0. \qquad (A\,7a,b)$$

As both Θ and U are odd in y, any even perturbation fulfils (A 7a) and (A 7b) and leaves a and c to be determined by (A 6a) and (A 6b). Odd solutions give $a = c = 0$, fulfil (A 6) but violate (A 7), and are therefore not of interest.

For any parameter values, one solution is given by $\tilde{\theta} = \tilde{\theta}_0$ (constant), $a = \tilde{\theta}_0 \cos\alpha$, and $\tilde{u} = \tilde{w} = c = \sigma = 0$. This is just a simple translation in bulk temperature, so it is not surprising that the mode is neutrally stable for all Ra. However, as is shown in Appendix B, some less trivial results can be obtained by considering perturbations of this mode for small but non-zero wavenumbers.

Let us continue by using the differential equations to eliminate the cases which can only give rise to decaying modes. Multiplying (A 3) with $\tilde{w}^*$ and integrating over y, it is shown, in analogy with (4.25), that any mode with a non-zero $\tilde{w}$ must be decaying. Corresponding manipulations on the remaining equations give

$$\frac{\sigma}{Pr}||\tilde{u}||^2 = -||\tilde{u}'||^2 + (\tilde{\theta}, \tilde{u})\cos\alpha, \qquad (A\,8)$$

$$\sigma||\tilde{\theta}||^2 = -||\tilde{\theta}'||^2 - (\tilde{u}, \tilde{\theta})RaS_x, \qquad (A\,9)$$

where $(a,b) = \int_{-1}^{1} ab^*\,\mathrm{d}y$ defines a scalar product, and $||a|| = (a,a)^{1/2}$ is the corresponding Hilbert norm.

For the special case of a horizontal enclosure, $\cos\alpha = 0$. Equation (A 8) then gives that $\sigma < 0$, or $\tilde{u}(y) \equiv 0$. Assuming the latter, (A 9) gives that $\sigma < 0$ or $\tilde{\theta}'(y) \equiv 0$. The latter alternative gives the already known solution with a constant $\tilde{\theta}$, for which $\sigma = 0$. Thus, there can be no instabilities with $k = m = 0$ for a horizontal enclosure.

Having treated the case $\cos\alpha = 0$, we henceforth assume $\cos\alpha \neq 0$, and replace S_x by $S\cos\alpha$. The linear combination RaS (A 8)+(A 9)* gives

$$\sigma\frac{RaS}{Pr}||\tilde{u}||^2 + \sigma^*||\tilde{\theta}||^2 = -RaS||\tilde{u}'||^2 - ||\tilde{\theta}'||^2. \qquad (A\,10)$$

The real part of this expression shows that if the stratification is natural ($S > 0$) there can only be decaying solutions. We therefore concentrate on cases with unnatural stratification ($S < 0$). Taking the imaginary part of (A 10), one has

$$\mathrm{Im}(\sigma)\left(\frac{RaS}{Pr}||\tilde{u}||^2 - ||\tilde{\theta}||^2\right) = 0, \qquad (A\,11)$$

which shows that σ is real whenever $S < 0$.

At this point, the even solutions for $\tilde{u}$ and $\tilde{\theta}$ must be found, assuming $S < 0$. With $B = (-RaS\cos^2\alpha)^{1/4}$, one obtains

$$\frac{\tilde{u}}{\cos\alpha} = A\frac{\cosh(B\mu\, y)}{\cosh(B\mu)} + C\frac{\cos(B\eta\, y)}{\cos(B\eta)} - (A + C), \tag{A 12}$$

$$\frac{\tilde{\theta}}{B^2} = -\frac{A + C}{s\sqrt{Pr}} + A\left(\frac{s}{\sqrt{Pr}} - \mu^2\right)\frac{\cosh(B\mu\, y)}{\cosh(B\mu)} + C\left(\frac{s}{\sqrt{Pr}} + \eta^2\right)\frac{\cos(B\eta\, y)}{\cos(B\eta)}, \tag{A 13}$$

where

$$s = \frac{\sigma}{\sqrt{Pr}B^2}, \quad A = \frac{\tan(B\eta)}{B\eta} - 1, \quad C = 1 - \frac{\tanh(B\mu)}{B\mu}, \tag{A 14}$$

$$\eta = \sqrt{-\frac{s}{2}\left(\sqrt{Pr} + \frac{1}{\sqrt{Pr}}\right) + \sqrt{1 + \frac{s^2}{4}\left(\sqrt{Pr} - \frac{1}{\sqrt{Pr}}\right)^2}}, \tag{A 15}$$

$$\mu = \sqrt{\frac{s}{2}\left(\sqrt{Pr} + \frac{1}{\sqrt{Pr}}\right) + \sqrt{1 + \frac{s^2}{4}\left(\sqrt{Pr} - \frac{1}{\sqrt{Pr}}\right)^2}}. \tag{A 16}$$

In deriving the above, all the equations and all the conditions on $\tilde{u}$ have been used. Finally, the condition $\tilde{\theta}'(1) = 0$ is applied to give the following relation, from which s can be solved for:

$$\mu A\left(\frac{s}{\sqrt{Pr}} - \mu^2\right)\tanh(B\mu) - C\eta\left(\frac{s}{\sqrt{Pr}} + \eta^2\right)\tan(B\eta) = 0. \tag{A 17}$$

One finds that criticality is given by $\tan B = \tanh B$, whose solutions are

$$B \approx 0, 3.927 + (n-1)\pi, \quad n = 1, 2, \ldots \tag{A 18}$$

In the first interval, $0 < B < 3.927$, there are no solutions with $s > 0$. In the second interval, there is one unstable mode – each time a new critical value is passed, one more mode becomes unstable. In conclusion, the condition for modes with $k = m = 0$ to be unstable is that

$$S < 0 \text{ and } B \equiv (-RaS\cos^2\alpha)^{1/4} > 3.927. \tag{A 19}$$

However, the zero wavenumber case is quite special because of the sudden appearance of integral conditions. For cases in which at least one of the wavenumbers is non-zero, no integral conditions are explicitly applied.

With $k \to 0$ and $m = 0$, $\tilde{w} \equiv 0$ for any mode which may grow. Scaling so that $\tilde{\theta} \sim O(1)$ makes $\tilde{v} \sim O(k)$, and $\tilde{u} \sim O(1)$, so that $\tilde{v} \to 0$ in the limit. $\tilde{u}$ is guaranteed from the continuity equation (4.16) to fulfil (A 6*a*), whereas (A 7*a*) is not generally satisfied. In the limit, one obtains the $k = m = 0$ case with only the condition (A 6*a*).

With $k = 0$ and $m \to 0$, one may again scale $\tilde{\theta}$ to be $O(1)$; then $\tilde{v} \sim O(m^2)$, $\tilde{w} \sim O(m)$, and $\tilde{u} \sim O(1)$, so that only $\tilde{u}$ and $\tilde{\theta}$ remain as $m \to 0$. However, for this case (A 6*a*) is generally *not* satisfied – instead (A 6*b*) is. In the limit, one has the $k = m = 0$ case with only the condition (A 6*b*). With the same definitions of s, η, and μ, the solution for the even modes now becomes

$$\frac{\tilde{u}}{\cos\alpha} = \frac{\cosh(B\mu\, y)}{\cosh(B\mu)} - \frac{\cos(B\eta\, y)}{\cos(B\eta)}, \tag{A 20}$$

$$\frac{\tilde{\theta}}{B^2} = \left(\frac{s}{\sqrt{Pr}} - \mu^2\right)\frac{\cosh(B\mu\, y)}{\cosh(B\mu)} - \left(\frac{s}{\sqrt{Pr}} + \eta^2\right)\frac{\cos(B\eta\, y)}{\cos(B\eta)}, \tag{A 21}$$

with s to be determined from

$$\mu\left(\frac{s}{\sqrt{Pr}} - \mu^2\right)\tanh(B\mu) + \eta\left(\frac{s}{\sqrt{Pr}} + \eta^2\right)\tan(B\eta) = 0. \tag{A 22}$$

This too gives the criticality conditions $\tan B = \tanh B$, but here there is an unstable mode even in the first interval. The case has been investigated previously by Lavine (1993), who did a stability analysis for zero wavenumbers of an arbitrary base solution of the form $\mathbf{u} = U(y)\mathbf{e}_x$, $\theta = Ax + Bz + F(y)$, between two plates with prescribed fluxes, and found an even mode to be destabilizing for all cases with top-heavy (unnatural) stratification. Integral conditions were not discussed in that work, so it was believed in SK that the results were not applicable. We have shown here, however, that even though Lavine's results are not strictly applicable for zero wavenumbers in the present case, they do describe the limit $k = 0$, $m \to 0$ correctly.

In numerical simulations with $m = 0$, and k small, we found instabilities for $B > 2.365$ (due to an odd mode), and for $B > 3.927$ for the first even mode. For $k = 0$ and m small, an even mode was found to be unstable for all $B > 0$. These findings all agree with the above analysis. Since the extent of the enclosure puts a limit on how small the smallest non-zero m may be, it may still be possible that solutions with unnatural stratifications can be stable in a box which is not too wide in z. Typically, however, the numerical results predict instability for m values as large as about one. Boxes such that m_{min} is less than $O(1)$ are possibly too thin for the base solution from SK to apply.

Appendix B. The horizontal, bottom-heated case with $k = 0, m \ll 1$

The following analysis has been made both manually and with use of computer algebra (Maple V, Char *et al.* 1991). A similar analysis of the corresponding problem in a porous medium can be found in Kimura, Vynnycky & Alavyoon (1995).

To be able to apply directly the base solution from SK, we specify the case as $\gamma = 225°, \alpha = 90°$ rather than the equivalent $\gamma = 45°, \alpha = -90°$, and obtain

$$\Theta = S_x x \underbrace{- \frac{y}{\sqrt{2}} + \frac{RaS_x^2}{4!}\left(\frac{y^5}{5} - \frac{2}{3}y^3 + y\right)}_{g(y)}, \tag{B 1}$$

$$U = \frac{S_x}{6}\left(y^3 - y\right), \tag{B 2}$$

$$S_x = \frac{3}{2Ra}\sqrt{14(R-45)}, \tag{B 3}$$

$$R = Ra/\sqrt{2}. \tag{B 4}$$

With $k = 0$ and $\alpha = 90°$, the perturbation equations read

$$\frac{\sigma}{Pr}\left(m^2\tilde{v} - \tilde{v}''\right) = -\tilde{v}'''' + 2m^2\tilde{v}'' - m^4\tilde{v} + m^2\tilde{\theta}, \tag{B 5}$$

$$\frac{\sigma}{Pr}\tilde{u} = \tilde{u}'' - m^2\tilde{u} - \frac{Ra}{Pr}U'\tilde{v}, \tag{B 6}$$

$$\sigma\tilde{\theta} = \tilde{\theta}'' - m^2\tilde{\theta} - Rag'\tilde{v} - RaS_x\tilde{u}, \tag{B 7}$$

with the boundary conditions

$$(\tilde{v}, \tilde{v}', \tilde{u}, \tilde{\theta}') = 0 \text{ at } y = \pm 1. \tag{B 8}$$

The third velocity component $\tilde{w}$ is not zero but equal to $\mathrm{i}\tilde{v}'/m$. In fact, $\hat{w}$ is typically much larger than $\hat{u}$ for the investigated mode – see figure 6(*a*).

Each of the eigenmodes can be expanded in a Taylor series around $m^2 = 0$:

$$\begin{pmatrix} \sigma \\ \tilde{v} \\ \tilde{u} \\ \tilde{\theta} \end{pmatrix} = \begin{pmatrix} \sigma_0 \\ \tilde{v}_0 \\ \tilde{u}_0 \\ \tilde{\theta}_0 \end{pmatrix} + m^2 \begin{pmatrix} \sigma_2 \\ \tilde{v}_2 \\ \tilde{u}_2 \\ \tilde{\theta}_2 \end{pmatrix} + m^4 \begin{pmatrix} \sigma_4 \\ \tilde{v}_4 \\ \tilde{u}_4 \\ \tilde{\theta}_4 \end{pmatrix} + O(m^6). \tag{B 9}$$

We wish to investigate cases in which the critical wavenumber goes to zero. A mode for which $m_c \to 0$ must have $\mathrm{Re}\{\sigma_0\} = 0$. From the study of the $k = m = 0$ case, we have seen that the only mode which fulfils this criterion is the one with $\tilde{\theta}_0$ constant and $(\sigma_0, \tilde{v}_0, \tilde{u}_0) = 0$. As this mode has $\mathrm{Re}\{\sigma_0\} = 0$ for all Ra, one must to go to higher orders to determine stability. At $O(m^2)$, the equations are

$$\tilde{v}_2'''' = \tilde{\theta}_0, \tag{B 10}$$

$$\tilde{u}_2'' = \frac{Ra}{Pr} U' \tilde{v}_2, \tag{B 11}$$

$$\tilde{\theta}_2'' = (1 + \sigma_2)\, \tilde{\theta}_0 + Rag' \tilde{v}_2 + RaS_x \tilde{u}_2, \tag{B 12}$$

with boundary conditions which follow from (B 8).

Solving (B 10) gives

$$\tilde{v}_2(y)/\tilde{\theta}_0 = \frac{1}{4!}\left(y^4 - 2y^2 + 1\right), \tag{B 13}$$

which, for (B 11), then gives

$$\tilde{u}_2''/\tilde{\theta}_0 = \frac{RaS_x}{6Pr4!}(3y^2 - 1)(y^4 - 2y^2 + 1) = \frac{RaS_x}{6Pr4!}(3y^6 - 7y^4 + 5y^2 - 1). \tag{B 14}$$

Integrating twice and applying the boundary conditions, one obtains

$$\tilde{u}_2(y)/\tilde{\theta}_0 = \frac{RaS_x}{6Pr4!}\left(\frac{3(y^8 - 1)}{8 \cdot 7} - \frac{7(y^6 - 1)}{6 \cdot 5} + \frac{5(y^4 - 1)}{4 \cdot 3} - \frac{1(y^2 - 1)}{2 \cdot 1}\right). \tag{B 15}$$

Equation (B 12) can now be integrated once to give

$$\frac{\tilde{\theta}_2'}{\tilde{\theta}_0} = (1 + \sigma_2)y + \frac{21(R - 45)}{16 \cdot 6Pr}\left(\frac{3(y^9 - 9y)}{9_1 7} - \frac{7(y^7 - 7y)}{7_1 5} + \frac{5(y^5 - 5y)}{5_1 3} - \frac{y^3 - 3y}{3_1 1}\right)$$

$$+ \frac{1}{4!}\left\{\frac{21(R - 45)}{16}\left(\frac{y^9}{9} - \frac{4y^7}{7} + \frac{6y^5}{5} - \frac{4y^3}{3} + y\right) - R\left(\frac{y^5}{5} - \frac{2y^3}{3} + y\right)\right\}, \tag{B 16}$$

where $n_k m$ denotes the product of the numbers from n to m with a step of k; this type of slightly innovative notation becomes useful as the complexity increases. The integration constant has been determined to zero, since $\tilde{\theta}_2'(1) + \tilde{\theta}_2'(-1) = 0$. From also requiring $\tilde{\theta}_2'(-1) = 0$, one has the surprisingly simple result

$$\sigma_2 = -\frac{R - 45}{30Pr}. \tag{B 17}$$

Since R must be larger than 45 for the convective base solution to be valid, the above

result means that, for every finite value of Pr, stability prevails for small enough m. Since real Prandtl numbers are always finite, one may be tempted to stop at this point. However, suppose that there are Rayleigh numbers such that $\sigma_4(R, Pr)$ has a positive value which does not vanish as $Pr \to \infty$. For such a Rayleigh number, with sufficiently high Pr, and a small m, the fourth-order term would dominate and cause an instability. We therefore continue the analysis one step further. Let us however do this only for the case $Pr \to \infty$. Then, from integrating (B 16),

$$\frac{\tilde{\theta}_2}{\tilde{\theta}_0} = \frac{y^2}{2} + \frac{21(R-45)}{16 \cdot 4!}\left(\frac{y^{10}}{10 \cdot 9} - \frac{4y^8}{8 \cdot 7} + \frac{6y^6}{6 \cdot 5} - \frac{4y^4}{4 \cdot 3} + \frac{y^2}{2 \cdot 1}\right) - \frac{R}{4!}\left(\frac{y^6}{6 \cdot 5} - \frac{2y^4}{4 \cdot 3} + \frac{y^2}{2 \cdot 1}\right) + C, \quad \text{(B 18)}$$

where C is a constant, which may be determined from a normalization condition. However, as such a condition should not affect σ, let us keep C undetermined. At $O(m^4)$, the equations are

$$\tilde{v}_4'''' = 2\tilde{v}_2'' + \tilde{\theta}_2, \quad \text{(B 19)}$$

$$\tilde{u}_4'' = \tilde{u}_2 = 0, \quad \text{(B 20)}$$

$$\tilde{\theta}_4'' = \sigma_4\tilde{\theta}_0 + \tilde{\theta}_2 + Rag'\tilde{v}_4 + RaS_x\tilde{u}_4. \quad \text{(B 21)}$$

From (B 20), we obtain $\tilde{u}_4 = 0$. In (B 19), $2\tilde{v}_2'' = y^2 - 1/3$ from (B 13), and one has, after integrating four times and applying the boundary conditions,

$$\frac{\tilde{v}_4}{\tilde{\theta}_0} = \left(P_6 - \frac{P_4}{3}\right) + \frac{P_6}{2} + \frac{21(R-45)}{16 \cdot 4!}\left(\frac{P_{14}}{10 \cdot 9} - \frac{4P_{12}}{8 \cdot 7} + \frac{6P_{10}}{6 \cdot 5} - \frac{4P_8}{4 \cdot 3} + \frac{P_6}{2 \cdot 1}\right) - \frac{R}{4!}\left(\frac{P_{10}}{6 \cdot 5} - \frac{2P_8}{4 \cdot 3} + \frac{P_6}{2 \cdot 1}\right) + CP_4, \quad \text{(B 22)}$$

where

$$P_n = \frac{y^n - (n/2)y^2 + n/2 - 1}{n_1(n-3)}, \quad \text{(B 23)}$$

so that $P_n(\pm 1) = 0$, $P_n'(\pm 1) = 0$, and $P_n'''' = y^{n-4}$ for $n \geqslant 4$.

σ_4 can now be found by integrating (B 21) from -1 to 1, and using the boundary conditions for $\tilde{\theta}_4$. One obtains, after a considerable amount of trivial calculation,

$$\sigma_4 = -\frac{30926}{230945} - \frac{671\,R}{2204475} + \frac{409\,R^2}{1964187225}, \quad \text{(B 24)}$$

an expression which is negative for small R, and positive for large R, so that a critical Rayleigh number results from solving $\sigma_4 = 0$, namely

$$R_c = \frac{597861 + 153\sqrt{33651489}}{818} \approx 1816, \quad \text{(B 25)}$$

which gives $Ra_c = \sqrt{2}R_c \approx 2568$. As can be seen from figure 9(d), this is a plausible limit for the numerical data to approach. Furthermore, both the expressions (B 24) and (B 17) were found to compare favourably with numerical calculations of σ.

Finally, let us devote a few lines to investigate whether or not the same type of analysis can be used to find the critical Rayleigh number for the *first* bifurcation (from a conductive to a convective solution). The reason why we expect

this to be possible is that the convective solution is in the form of a single cell. Although one would rather think of the convective solution as a result of an instability with $m = 0, k \to 0$, than one with $k = 0, m \to 0$, the two limits are equivalent for this case. The conductive base solution is $\theta = y/\sqrt{2}, u = 0, S_x = 0$. Again, it is only the zeroth-order solution with zero velocities and $\tilde{\theta}_0$ constant which need be considered. Furthermore, $\tilde{v}_2$ becomes the same as above. Integrating (B 12) from -1 to 1 and applying the boundary conditions on $\tilde{\theta}_2$ gives

$$\sigma_2 = -1 + \frac{R}{45}, \tag{B 26}$$

so that $R_c = 45$, in agreement both with the numerical stability analysis of Sparrow *et al.* (1963), and with the existence condition for the bifurcated solution from SK.

Appendix C. Perturbation equations in the boundary-layer limit

For large values of $\beta = (RaS\cos^2\alpha/4)^{1/4}$, U has a boundary layer of thickness $O(\beta^{-1})$, and amplitude $O(\beta^{-3}\cos\alpha)$; the boundary layer for Θ is of equal thickness, but with the different amplitude $O(\beta^{-1})$. To avoid numerical difficulties, the following rescaled variables were introduced:

$$U_b = \beta^3 U/\cos\alpha, \quad f_b = \beta f, \quad \tilde{V} = \beta^3\tilde{v}, \quad \tilde{\Omega}_y = \beta^2\tilde{\omega}_y, \quad \tilde{T} = \beta\tilde{\theta}, \tag{C 1a–e}$$

$$Y = \beta(1+y), \quad \sigma_b = \sigma/\beta^2, \quad K = k/\beta, \quad M = m/\beta. \tag{C 1f–i}$$

With this scaling, one has

$$U_b = -\frac{1}{2}\left(\frac{\lambda_1+\lambda_2}{2} - S\sin\alpha\right)\mathrm{e}^{-Y}\sin Y + \frac{\lambda_2-\lambda_1}{8\beta}\left\{(2\beta-1)\,\mathrm{e}^{-Y}\sin Y - 1 + \mathrm{e}^{-Y}\cos Y\right\} + O(\mathrm{e}^{-2\beta}), \tag{C 2a}$$

$$f_b = -\left(\frac{\lambda_1+\lambda_2}{2} - S\sin\alpha\right)\mathrm{e}^{-Y}\cos Y + \frac{\lambda_2-\lambda_1}{4}\left\{\left(2-\frac{1}{\beta}\right)\mathrm{e}^{-Y}\cos Y + \frac{1}{\beta^2} - \frac{1}{\beta} - \frac{\mathrm{e}^{-Y}\sin Y}{\beta}\right\} + O(e^{-2\beta}). \tag{C 2b}$$

The new variables obey the following equations:

$$\frac{\sigma_b}{Pr}\left(Q\tilde{V} - \tilde{V}''\right) = -\tilde{V}'''' + (2Q + AKU_b)\,\tilde{V}'' - AKU_b''\tilde{V} - Q\,(Q + AKU_b)\,\tilde{V} + \mathrm{i}K\tilde{T}'\cos\alpha + Q\tilde{T}\sin\alpha, \tag{C 3a}$$

$$\frac{\sigma_b}{Pr}\tilde{\Omega}_y = \tilde{\Omega}_y'' - (Q + AKU_b)\,\tilde{\Omega}_y - AMU_b'\tilde{V} + \mathrm{i}M\tilde{T}\cos\alpha, \tag{C 3b}$$

$$\sigma_b\tilde{T} = \tilde{T}'' - \left(Q + \frac{4\mathrm{i}KU_b}{S\cos\alpha}\right)\tilde{T} - \frac{4\mathrm{i}K\tilde{V}'}{Q\cos\alpha} + \frac{4\mathrm{i}M\tilde{\Omega}_y}{Q\cos\alpha} - \left(f_b' + S\sin\alpha\right)\frac{4\tilde{V}}{S\cos^2\alpha}, \tag{C 3c}$$

where

$$Q = K^2 + M^2, \quad A = \frac{4\mathrm{i}}{PrS\cos\alpha}, \quad {}' = \frac{\mathrm{d}}{\mathrm{d}Y}. \tag{C 4a–c}$$

The boundary conditions at $Y = 0$ are

$$\tilde{V} = \tilde{V}' = \tilde{\Omega}_y = \tilde{T}' = 0. \qquad \text{(C 5}a\text{–}d\text{)}$$

At the right-hand end of the region solved for, which is here a point in the interior, the boundary conditions are not immediately given, and different treatments can be thought of. As the perturbations were seen to decay exponentially to zero in the interior, we chose a simple treatment, and applied the boundary conditions (C 5) at the right-hand boundary as well. The position of the right-hand boundary was adjusted to make the errors due to the arbitrarily chosen boundary conditions negligible. Typically, it was enough to put the boundary at $Y = 30$. For a test case, it was also checked that a change in one of the boundary conditions from $\tilde{T}' = 0$ to $\tilde{T} = 0$ had no effect on the modes of interest. There are also false modes, which have their main variation near the right-hand boundary, but these were all found to be stable, and were therefore sorted away automatically.

REFERENCES

Bark, F. H., Alavyoon, F. & Dahlkild, A. A. 1992 On unsteady free convection in vertical slots due to prescribed fluxes of heat or mass at the vertical walls. *J. Fluid Mech.* **235**, 665–689.

Bejan, A. 1979 Note on Gill's solution for free convection in a vertical enclosure. *J. Fluid Mech.* **90**, 561–568.

Bejan, A. 1984 *Convection Heat Transfer*. Wiley-Interscience.

Bergholz, R. F. 1978 Instability of steady natural convection in a vertical fluid layer. *J. Fluid Mech.* **84**, 743–768.

Birikh, R. V., Gershuni, G. Z., Zhukovitskii, E. M. & Rudakov, R. N. 1969 Stability of the steady convective motion of a fluid with a longitudinal temperature gradient. *Appl. Math. Mech.* **33**, 937. (Russian original in *Prikl. Mat. i Mekh.* **33**, 958.)

Busse, F. H. 1978 Nonlinear properties of convection. *Rep. Prog. Phys.* **41**, 1929–1967.

Chait, A. & Korpela, S. A. 1989 The secondary flow and its stability for natural convection in a tall vertical enclosure. *J. Fluid Mech.* **200**, 189–216.

Chandrasekhar, S. 1961 *Hydrodynamic and Hydromagnetic Stability*. Oxford University Press.

Char, B. W., Geddes, K. O., Gonnet, G. H., Leong, B. L., Monagan, M. B. & Watt, S. M. 1991 *Maple V Library Reference Manual*. Springer.

Dahlquist, G., Björck, Å. & Anderson, N. 1974 *Numerical Methods*. Prentice-Hall.

Davis, S. H. 1967 Convection in a box: linear theory. *J. Fluid Mech.* **30**, 465–478.

Davis, S. H. 1990 Hydrodynamic interactions in directional solidification. *J. Fluid Mech.* **212**, 241–262.

DiPrima, R. C. & Habetler, G. J. 1969 A completeness theorem for non-selfadjoint eigenvalue problems in hydrodynamic stability. *Arch. Rat. Mech. Anal.* **34**, 218–227.

Drazin, P. G. & Reid, W. H. 1981 *Hydrodynamic Stability*. Cambridge University Press.

Elder, J. W. 1965 Laminar free convection in a vertical slot. *J. Fluid Mech.* **23**, 77–98.

Gill, A. E. & Davey, A. 1969 Instabilities of a buoyancy-driven system. *J. Fluid Mech.* **35**, 775–798.

Golub, G. H. & Loan, C. F. van 1996 *Matrix Computations*, 3rd edn. John Hopkins University Press.

Hart, J. E. 1971 Stability of the flow in a differentially heated inclined box. *J. Fluid Mech.* **47**, 547–576.

Joseph, D. D. 1976 *Stability of Fluid Motions II* (Chapter VIII : 56, 57). Springer.

Kimura, S., Vynnycky, M. & Alavyoon, F. 1995 Unicellular natural circulation in a shallow horizontal porous layer heated from below by a constant flux. *J. Fluid Mech.* **294**, 231–257.

Koschmieder, E. L. 1993 *Bénard Cells and Taylor Vortices* (Chapters 6 & 7). Cambridge University Press.

Lavine, A. 1993 On the linear stability of mixed and free convection between inclined parallel plates with fixed heat flux boundary conditions. *Intl J. Heat Mass Transfer* **36**, 1373–1381.

Le Quéré, P. 1990*a* Transition to unsteady natural convection in a tall water-filled cavity. *Phys. Fluids* A **2**, 503–515.

Le Quéré, P. 1990*b* A note on multiple and unsteady solutions in two-dimensional convection in a tall cavity. *Trans. ASME: J. Heat Transfer* **112**, 965–974.

Le Quéré, P. & Pécheux, J. 1989 Numerical simulations of multiple flow transition in axisymmetric annulus convection. *J. Fluid Mech.* **206**, 517–544.

Leal, L. G. 1992 *Laminar Flow and Convective Transport Processes.* Butterworth-Heinemann.

Lundbladh, A. & Johansson, A. V. 1991 Direct simulation of turbulent spots in plane Couette flow. *J. Fluid Mech.* **229**, 499–516.

Patterson, J. & Imberger, J. 1980 Unsteady natural convection in a rectangular cavity. *J. Fluid Mech.* **100**, 65–86.

Pellew, A. & Southwell, R. V. 1940 On maintained convective motion in a fluid heated from below. *Proc. R. Soc. Lond.* A **176**, 312–343.

Rayleigh, Lord 1916 On convection currents in a horizontal layer of fluid, when the higher temperature is on the under side. *Phil. Mag.* (6) **32**, 529–546.

Reddy, S. C. & Henningson, D. S. 1993 Energy growth in viscous channel flows. *J. Fluid Mech.* **252**, 209–238.

Sparrow, E., Goldstein, R. & Jonsson, V. 1963 Thermal instability in a horizontal fluid layer: effect of boundary conditions and non-linear temperature profile. *J. Fluid Mech.* **18**, 513–528.

Sundström, L.-G. & Bark, F. H. 1995 On morphological instability during electrodeposition with a stagnant binary electrolyte. *Electrochimica Acta* **40**, 599–614.

Sundström, L.-G. & Kimura, S. 1996 On laminar free convection in inclined rectangular enclosures. *J. Fluid Mech.* **313**, 343–366 (referred to herein as SK).

Vest, C. M. & Arpaci, V. S. 1969 Stability of natural convection in a vertical slot. *J. Fluid Mech.* **36**, 1–15.

Wang, T.-M. & Korpela, S. A. 1992 Secondary instabilities of convection in a shallow cavity. *J. Fluid Mech.* **234**, 147–170.